Guilhem Hoareau
Laboratoire des Fluides Complexes et leurs Réservoirs
IPRA-Université de Pau et des Pays de l'Adour
Avenue de l'Université
64000 PAU
France
Phone : +33 (0)5 59 40 73 40
guilhem.hoareau@univ-pau.fr

Pau, Tuesday 3rd of June 2025

To Geochronology Associate Editor,

Dear Associate Editor,

Please find a new version of manuscript egusphere-2024-2366 "The virtual spot approach: a simple method for image U-Pb carbonate geochronology by high-repetition rate LA-ICP-MS", by Hoareau et al.

As requested by the reviewers, the manuscript has been modified significantly.

- The text was partly rewritten, including (i) a more direct comparison between results obtained with Tera-Wasserburg and Wetherill regressions, (ii) a more precise description of the results, and (iii) an explanation of the proper way to use the approach.

- Two figures were added (comparison between TW and W regressions for all samples – Fig.3, and a guideline for the use of the approach – Fig. 11)

- All figures were improved with bigger fonts and colour scales adapted to colour blind readers

- The supplement (Zenodo) now includes a new figure as requested by the reviewers.

We hope that these modifications will be appreciated and will allow this work to be published in Geochronology.

Sincerely,

Guilhem Hoareau

We thank the reviewers for their very detailed comments, which prompted us to reflect deeply on several of the points raised. We hope that our responses are sufficiently precise and well-supported. The original comments are in bold font, and the responses in normal font.

R1

General Comments:

This manuscript presents an approach to reduction of large quantities of spatially characterized isotopic data obtained by raster scans of samples using LA-ICPMS. Image reduction programs already exist. The main novel feature of this one seems to be the ability to average data from virtual spots in order to achieve an optimal balance between precision and spatial resolution. As such, it is of potential use to a large number of geochemists and geochronologists. I found it to be very interesting, although I have no experience in using a femtosecond laser and have never tried elemental imaging.

We thank you for this overall positive comment.

Specific Comments:

The manuscript could use a more extensive and clearer discussion of limitations and how these might be improved.

The main limitation of our approach concerns samples with low U and/or Pb concentrations (low number of counts), for which biased ages may be obtained depending on the regression method used (TW or Wetherill). These points are discussed in more detail below. We will place greater emphasis on this issue and propose a workflow for applying the approach, following a suggestion from Barbara Kunz and Igor Figueiredo (reviewers 2).

The authors use a single collector mass spectrometer so masses are measured at different times. The lateral movement between mass scans is about 1.4 mic while the pulse separation is about 0.05 mic. However, spatial resolution of data should be mainly limited by the ca. 0.6 sec transfer function (washout time) of ablated material into the plasma (in contrast to line 465), which covers a range of about 15 mic of beam movement along a scan. The observed distribution of isotopic ratios in the direction of a scan should be the actual distribution convoluted with the transfer function of the instrument. This would cause data variations along a scan at a scale lower than about 15 mic to be smeared together by the response time of the instrument, which is much broader than the distance covered by a mass sweep (1.4 mic).

We agree that from an LA-ICP-MS imaging quality perspective, not accounting for the longer washout time when choosing the mass sweep duration (whether averaged to a higher value or not) can result in image smearing. However, Figure 2 shows that this smearing remains limited with a washout time of approximately 500 ms. Visual image resolution is not the primary objective in this case, although, of course, the highest possible resolution is desirable. The guiding principle here is to retain all measurements (each mass scan), even if signal mixing occurs, because the goal is to generate virtual spots, by analogy with static spot ablations. Signal mixing is common in static ablation, where a more homogeneous signal is sought to improve statistical reliability. In such cases, each ablation takes a different volume of the sample, but the overall signal is mixed/homogenized. A higher sampling time improves the statistical uncertainty on the mean, which decreases with the square root of N. In the case of the images produced here, the signal will not be as homogeneous as in static ablation, since the system's washout time remains relatively short (500 ms). This value represents a compromise between limiting image smearing along a line and obtaining a sufficiently reliable uncertainty on the mean. It should be noted that averaging the mass scans can have a beneficial effect on age accuracy for low-concentration samples, as illustrated by the example of C6-265-D5. Conversely, the example of BH14—based on both the results from Hoareau et al. (2021), who used an averaged mass scan of 540 ms, and the present study—shows that results are more satisfactory without averaging the mass scans. Therefore, for each sample, it is reasonable to test multiple configurations (with and without averaging) to select the most accurate and precise one.

Therefore, defining the mass sweep as a pixel seems a bit misleading. Pixels, in the sense of a fundamental area scale at which independent values can be measured, are really more like the size of the spots but they vary along a continuum so it might be better to avoid the term pixel altogether.

We initially used the term *pixel* in its general definition, which goes beyond isotopic imaging, namely 'the smallest addressable element in a raster image' (Wikipedia). This definition is independent of any potential signal correlation between adjacent pixels and is easily understandable, even for non-specialist readers. As an example, in the case of digital images, increasing the resolution from 100 px × 100 px to 200 px × 200 px multiplies the number of pixels by four based on the original image, with the new pixels necessarily being correlated (in terms of colour). Nevertheless, they are still referred to as pixels.

We prefer to retain the term *pixel* as a clear and accessible term, while adding a clarification in the Methods section of the manuscript to address the issues you raise from the perspective of LA-ICP-MS imaging.

The relatively slow instrument response time is largely the result of using a nebulizer chamber where carrier He and makeup Ar are mixed before injection into the plasma. Response time can be significantly lowered by the use of a

modified, commercially available, quartz injection tube where mixing between the He carrier gas and Ar occurs within the plasma. Further improvement would require the use of a multi-collector or time of flight mass spectrometer in which signals for different masses are effectively measured simultaneously.

We fully agree with these remarks, which go beyond the scope of the present study. The instrumentation used is not necessarily the most efficient for LA-ICP-MS imaging, and we hope to benefit from more advanced setups in the future.

The scale of observable compositional variations across (rather than along) scans will be limited by the beam size (25 mic).

Yes. To be more precise, the beam size is 15 µm but galvanometric scanners allow to rapidly move the beam to generate a 25 µm-width line, but the result is the same.

It should also be noted that although the scan line is claimed to have a depth of 40 mic at 500 Hz, the troughs should have a V-shaped profile for non-overlapping lines so the average depth would be 20 mic. One should therefore be mapping triangular segments beneath the surface. This should of course affect ablation bias so standards need to be analyzed the same way.

We fully agree. The troughs broadly have a V-shape, with the highest depth reaching about 40 µm as measured with a digital microscope. This maximum value is not an average. It is this maximum penetration depth that is critical for us when analysing thin samples, which must not be traversed. In any case, we always use strictly similar parameters to analyse the standards.

A more fundamental problem is the fact that regression of relatively imprecise ratios produces ages that can be significantly different using the Wetherhill plot and the more commonly used Tera-Wasserburg (T-W) plot.

We agree. This is clearly shown by the example of sample C6-265-D5.

I assume the reason is that one measures counts on the masses but one plots and calculates with ratios of these counts. Errors in the numerator mass count will propagate linearly whereas those in the denominator mass count will only propagate linearly to first order so second order effects become important when the relative error is large. This was the main reason that I developed the approach of regressing signals in a 3D space where the Wetherhill solution generally agrees most closely with the 3D solution for poorly radiogenic data sets and both disagree for highly radiogenic data sets (see Davis and Rochan-Banaga, 2021, Fig. 5).

Your comment is very interesting; indeed, we did not address this specific point, which you discuss in detail in Davis and Rochin-Banaga (2021). Clearly, this was not an aspect we intended to cover here, as we are not able to provide further insights beyond those you have already offered. We tested sample C6-265-D5 using the Brama2.0 software developed by Liu et al. (2023), which is a Python-based equivalent of UtilChron. We were also unable to obtain a satisfactory age. The initial regression in Wetherill space yields an age of around 115 Ma, whereas the Bayesian solution gives an age of approximately 63 Ma. This discrepancy is not resolved by averaging the mass sweeps in groups of 8, for instance (as done in Hoareau et al. 2021).

The reason can be visualized by considering that non-linear variations in the denominator isotope in T-W plots (^{206}Pb) will bias data along a diagonal, which usually is at a high angle to the mixing line (isochron), whereas in the Wetherhill plot the denominator isotopes are from U, which is usually the largest peak (lowest error) and the common Pb end member is at infinity so non-linear variations will tend to be sub-parallel to the mixing line unless the datum is very radiogenic. The manuscript demonstrates this clearly but does not offer any discussion on how to effectively deal with it. One way would be to do regressions in 3D but there may be ways of correcting for it in 2D.

In the manuscript, we propose resolving these age inconsistencies between TW and Wetherill regressions by averaging the number of mass scans (smoothing), even though this results in larger individual uncertainties for the virtual spots. For easily datable samples (e.g., ARB20-2D or BH14), TW and Wetherill ages agree within uncertainties, and smoothing is unnecessary: it does not change age values but increases their uncertainty. For low-concentration samples (e.g., C6-265-D5), smoothing helps eliminate erratic isotopic ratios caused by too many zero or negative counts for ^{207}Pb and ^{206}Pb, which usually result in overly high $^{238}U/^{206}Pb$ and $^{207}Pb/^{206}Pb$ ratios in TW diagrams. These ratios bias the regression towards a shallower slope and thus a younger age. We agree that this effect should be less pronounced in Wetherill regressions. However, the C6-265-D5 example shows that averaging the mass scans alters both the TW and Wetherill ages, which then converge towards a common value. We consider this convergent value more reliable, although it should ideally be tested on samples of known age.

To further expand on this very interesting issue, we present here a point we discussed in 2024 with Pieter Vermeesch, concerning both the age differences between TW and Wetherill regressions and the discrepancies in results between Isoplot and IsoplotR. Taking sample C6-265-D5 as an example, without averaging the mass scans and using virtual spots of 100 µm × 100 µm across the entire image (n = 42), the age obtained with Isoplot from $^{206}Pb/^{238}U$ and $^{207}Pb/^{235}U$ ratios in Wetherill space is 140 ± 25 Ma, identical to the age calculated using IsoplotR. In contrast, the age obtained from $^{238}U/^{206}Pb$ and $^{207}Pb/^{206}Pb$ ratios in TW space using Isoplot is 84 ± 16 Ma, which is higher than the age proposed by IsoplotR (76 ± 17 Ma). This discrepancy stems from differences in the regression methods used by the two software packages:

1. In Isoplot, regressions—whether in TW or Wetherill space—are performed using the York algorithm. The software can compute four different ages for a single sample depending on the chosen ratios and coordinate space.
2. In contrast, IsoplotR always performs regressions in Wetherill space, regardless of the input ratios (whether $^{207}Pb/^{235}U$ and $^{206}Pb/^{238}U$, or $^{238}U/^{206}Pb$ and $^{207}Pb/^{206}Pb$). The software, which uses the York and/or Ludwig (1998) algorithm (both yielding identical results), thus calculates only two ages. The results are then simply displayed in either the TW or Wetherill plot, depending on the user's choice.

Therefore, if one uses $^{238}U/^{206}Pb$ and $^{207}Pb/^{206}Pb$ ratios to perform a Wetherill regression in Isoplot, the resulting value will be identical to the one obtained in TW coordinates using IsoplotR, i.e., 76 ± 17 Ma. For easily datable samples such as BH14, both software tools yield identical or nearly identical results regardless of the chosen method. The discrepancies observed in bad samples such as C6-265-D5, as noted by Pieter Vermeesch, illustrate that "*both age estimates are likely biased and wrong*". In our view, comparing TW and Wetherill age estimates should become a systematic prerequisite to assess the robustness of U-Pb geochronology results in general.

The best application that I can think of for this method would be WC1. This is an excellent standard because of its relatively old age and high U concentration but shows evidence of not being homogeneous in age based on the high ID-TIMS age error (2.7%) and the work of Guilong et al (2020, https://doi.org/10.5194/gchron-2019-20). If it were possible to isolate the predominate phase, this would be a much more useful standard.

This is an interesting comment, although we believe that our approach may also prove useful for other types of samples.

Technical corrections:

If one choses not to indent paragraphs there should be a space left between them, as well as between references.

OK. We will check this in the new version.

In some places I found the phasing unclear or ambiguous. Suggestions for improvement are made on an annotated copy.

Thank you for the time spent for the phrasing. We will try to follow all suggestions made.

The authors refer to Wetherhill Concordia plots as 'concordia' and the inverse (but more commonly used in this application) Tera-Wasserburg concordia plot

as T-W. This is confusing because both are concordia plots. It would be better to refer to T-W and W plots.

We agree that it is unclear as presented. We will make the appropriate changes.

Line 62:

Presumably the authors mean 207Pb/235U, but why would one want to use this ratio, rather than the more precise 206Pb/238U ratio as a criterion for sorting? They both encode the same information (age and radiogenicity).

We suggest to directly contact Kirsten Drost to discuss this, as it is not our proper work. The problem with $^{206}Pb/^{238}U$ sorting is that it tends to overweight outliers with high $^{238}U/^{206}Pb$ ratios in the TW space, resulting in results biased towards too young ages.

Line 73:

The 3D regression also allows for editing outliers. This aspect is a separate problem from the best regression approach as discussed above.

We agree. However, we wanted to emphasize that "bad quality samples" may also give biased results with the Bayesian approach: the prior estimate is obtained with a York regression on individual pixel values to which uncertainties are added from Poisson statistics. If the Isoplot estimate is biased for the reasons exposed above, the Bayesian result might be biased too, as we understand from our experience with this approach.

Lines 125, 129, Table 1:

A better use of English would be to refer to line width (rather than height) as the diameter of the laser beam and line length (rather than width) as the scanning distance. Otherwise it can be confusing to the reader.

OK. We will change the terms in the next version of the manuscript.

R2

General Comments:

The manuscript presents a novel approach to obtaining U-Pb ages of carbonates using isotopic maps and guided by statistical approaches to obtain the best age in what can be considered virtual spots. This is an interesting approach, and we can see the benefits the approach can have. The authors present a large amount of data from a number of samples (some of which have been previously dated for comparison).

Specific Comments:

- **In the introduction, the manuscript heavily relies on references and comparison with other studies, which when one isn't familiar with all of them makes reading and following the arguments a bit difficult. Particularly as the reader doesn't know the details of the approach this paper takes at that point in the text. Therefore, we wonder if some of this might be better suited for the discussion instead of the introduction. We would welcome it if the abstract and the introduction would focus a bit more on the rationale for using this approach. Why is this new method needed, what is the overall problem, that justifies using the approach the authors present? The text says that the ages are similar to the traditional approach but that the uncertainties can be worse. So, the authors should be clearer what the advantage of this method over the other methods is.**

In the introduction, we will aim to clarify the relevance of using isotopic imaging for geochronology, as well as the need to develop approaches that yield the most reliable ages possible. However, we do not intend to engage in a comparison of 'which data processing model is the best.' In this contribution, we present an alternative approach to those already published. We do not wish to portray our approach as a breakthrough that renders previous work obsolete. On the contrary, our method was developed through reflections inspired by existing approaches. As stated in the introduction and the discussion, each method has its own strengths and weaknesses, and ours is no exception. Through this contribution, above all we aim to share with the community the progress of our ongoing work on LA-ICP-MS map processing for U-Pb geochronology.

After stating here in the methods that some samples have been treated differently none of this is mentioned afterwards in the results of discussion. Even if it doesn't make a difference. It would be important to mention that explicitly. If it does make a difference could some of the results be influenced by this and if yes how?

We suppose you give details of the different treatments in the following lines.

- **Line 128: Why was the laser frequency changed from 100 to 500 Hz, please explain this change and the advantage of using one over the other. Additionally, can you detail if and what change this has on the results?**

In this contribution, we draw on analytical results obtained over the course of several years and across numerous research projects. By default, we work at 500 Hz on thick samples (mounts) to maximize signal intensity. With this setup, we typically obtain 100k–200k cps for ^{238}U on the NIST SRM 614. The work performed at 100 Hz (ARB20-2D) was conducted on a thin section. The only reason for this was the shallower ablation depth, which prevents drilling through the section. It is of course associated with lower number of counts (70–100k cps). This change in repetition rate has no impact on how the data are processed using our method.

- **Line 137: For sample BH14 only Ar was used as a carrier gas. It has been shown by Eggins et al., 1998 that Ar and He have quite different transport qualities. How did the use of only Ar as a carrier gas influence the results?**

We cannot answer. BH14 was one of the very first samples analysed using imaging in our laboratory. We initially tested Ar to assess the feasibility of carbonate imaging, knowing that the washout time would be longer. Later, switching to He was motivated by its faster washout time, which provided greater responsiveness, although it also led to slightly more signal variability (based on standards WC1 and NIST), without any significant impact on the quality of the results in terms of precision and accuracy. We did not repeat tests using Ar after the analyses of BH14.

- **Line 149: Why was NIST SRM 614 used after 2020 and 612 before 2020? Are there any differences in the results or uncertainties?**

Initially, we worked with NIST SRM 612 for two main reasons: (i) it was already used to tune the spectrometer at the beginning of each session, making it a practical choice. Our custom-built ablation cell does not allow for multiple standards alongside the unknown sample, so keeping NIST SRM 612 saved time; and (ii) tests using NIST SRM 614 revealed slight inhomogeneities in $^{206}Pb/^{238}U$ ratios (as has been reported elsewhere). However, since the concentrations in NIST SRM 614 are closer to those found in natural calcite, its use for calibration appears more appropriate and justifies the switch. Objectively, we did not observe any significant differences depending on the standard used. It is also worth noting that some research groups use NIST SRM 612 for Pb/Pb ratio correction (e.g., Parrish et al., 2018).

- **Use of rainbow colour maps. Jet or rainbow colour maps have been shown to be not a good choice. Both in terms of accessibility (colour**

blind and other sight impairments) the rainbow scheme is also misleading normal normal-sighted people due to a higher sensitivity of the human eye for certain colours which leads to a visual bias. Therefore, it should not be used:

https://blogs.egu.eu/divisions/gd/2017/08/23/the-rainbow-colour-map/

Have a look here for alternative suggestions https://www.fabiocrameri.ch/colourmaps/

Thank you for your suggestion. We will revise the color schemes in the figures to ensure they are accessible to visually impaired readers.

- **The comparison of the ages already determined by other studies (AUG-B6, BH14, DBT, Senz7) and this manuscript isn't very clear. In section 5.1.1. it is mentioned, but in none of the tables or figures (despite a reference to it) is it shown clearly.**

The reference ages are provided in Table 2 along with the appropriate citations, as well as in Section 2. In Section 5.1.1, Table 2 is indeed not referenced, which we will correct.

- **A lot of the ages are quoted without external error propagation. How much would external uncertainty add? I assume a good amount of external uncertainty comes from the standards? What other sources are there and what is the justification to ignore them? When comparing ages from previous studies with this one external error propagation would be needed to understand the full extent of how they compare to each other.**

We suppose that what you call 'external error' is that coming from the standards (referred to as "External 2σ err req'd (each pt)" in Isoplot). In our current procedure this additional uncertainty is directly calculated by Iolite4 from NIST SRM 614, based on the paper of Paton et al 2010 (reference will be added to the Methods section for clarity). Note that since we follow closely the recommendations of Horstwood et al. (2016), such excess variance is added directly onto the data points (ellipses) and not onto the final age. Additional systematic uncertainty includes a long-term variance (2%) that should allow confident comparison with ages obtained by other studies.

- **In section 5.2 the choice of data processing approach shows large (up to 50 Ma) variations in age (shown in figure 6 as well). How should a user choose which one to use? In the text, the authors mention that they chose the one closer to the expected age. But what if one doesn't know the expected age? Wouldn't this also mean that people might reject the 'true' age because they didn't expect it?**

Thank you for your pertinent observation. We fully agree that obtaining reliable ages from low-concentration samples—such as C6-265-D5—remains one of the main limitations of the approach presented in this study. It is indeed essential to verify whether a given sample is suitable for accurate U-Pb dating using this method. We address this issue in detail in our response to Don Davis, but we will also clarify it further in the revised manuscript. Specifically, we propose including a more explicit discussion outlining the importance of systematically comparing ages obtained from both Tera-Wasserburg and Wetherill regressions, in addition to evaluating conventional statistical parameters such as the MSWD. If the TW and Wetherill concordia ages do not overlap within their respective uncertainties, this should be taken as a strong indicator of potential bias and sample unreliability. Our tests suggest that, in such cases, averaging (smoothing) the mass scans can help reduce the impact of erratic isotope ratios, leading to better agreement between TW and Wetherill ages. However, this comes at the cost of reduced precision due to the lower number of pixels per virtual spot. Whether this trade-off improves accuracy remains an open question. The example of C6-265-D5 is promising, as the age obtained after smoothing aligns well with independent geological constraints. That said, we acknowledge that further work is needed to assess the robustness of this approach across a broader range of low-concentration samples. We will add this discussion to the revised manuscript, both to clarify the limitations and to outline potential future improvements.

- **In section 5.3.1 line 348 the authors refer to a map of sample Cot02a that has more precise ages, but then say it isn't presented here? Why is that? Why not at least provide this in the supplement?**

We did not include the second map (produced during the same analytical session) in the main manuscript because our objective here was to focus on the potential of isotopic mapping to distinguish and date multiple generations of calcite—specifically, matrix versus fracture domains. The second map simply does not contain any fracturing and therefore does not contribute directly to this particular discussion. However, we agree that providing it may offer useful context, and we will include this additional map in the supplement.

- **In lines 427-428: The sentence 'In the case of reliable samples, it is expected that the position of the spots does not influence the calculated ages.' What would you consider a reliable sample?**

Thank you for pointing this out. We agree that the definition of a "reliable sample" should be clarified. In the revised manuscript, we will specify that by "reliable sample," we refer to a sample with a homogeneous age and common Pb composition, sufficiently high U and Pb concentrations, and a wide enough range in isotopic ratios to allow for both accurate and precise U-Pb dating. We will revise the phrasing accordingly in the relevant section.

- **What if your sample isn't reliable, can you still use the approach?**

In our view, the proposed approach is particularly useful for assessing the reliability of a sample for geochronological purposes. As a first step, it is important to verify the consistency of the weighted mean ages obtained across the dataset. To support this, we propose to include a supplementary figure showing the weighted mean ages calculated for the different samples, based on 100 µm x 100 µm virtual spots in both the Tera-Wasserburg and Wetherill spaces. However, consistency alone is not sufficient to guarantee accuracy. As demonstrated by the C6-265-D5 example, coherent age estimates can still be biased. Therefore, as a second step, we believe it is essential to compare TW and Wetherill ages, which should agree within uncertainty. As discussed above, a discrepancy between these two regressions indicates potential bias and questions the reliability of the sample. We will expand the discussion on these points in the section addressing the limitations of our approach. Please also see below for additional details.

- **We would appreciate it if the authors could provide a bit more information on the limitations of this method. Particularly as carbonates can be complex in their formation and thereby age pattern. We would also appreciate it if the authors would touch on potential user biases that could be introduced when choosing one approach over another. It has been shown that data reduction and the choice of approach can make a difference in the final result. Particularly here with the possibility of choosing many virtual spots and statistical approaches, some clear guidelines for the reader would be helpful.**

In our virtual spot approach, we propose several strategies to obtain ages: the moving grid, sub-image, and Rectis methods. Among these, the moving grid is the primary and recommended approach and should always be used as the first step. We will clarify this point in the discussion. The sub-image and Rectis methods are complementary but optional. Specifically, the sub-image method presented here is more of a proof of concept, demonstrating the potential to date very small areas using our approach. Nonetheless, it can also contribute additional age constraints for larger samples through a weighted mean of sub-image results.

To help guide users through the most appropriate use of our method and to mitigate its main limitation—namely, the risk of biased ages for challenging samples—we will add a workflow to the discussion. This will be presented both in text and as a graphic and will outline a logical sequence of steps:

1. Initial age calculation: Calculate a series of ages using 100 µm x 100 µm virtual spots in both TW and Wetherill spaces.

2. Check consistency: Assess (i) internal consistency of the ages in each space, and (ii) agreement between TW and Wetherill ages. Both conditions must be satisfied. If not, investigate the potential causes (e.g., low U/Pb concentrations, insufficient isotopic spread, multiple age populations). The datability of the sample should be questioned.
3. Age selection:
   (a) If the ages are consistent, select the most statistically robust result (e.g., lowest MSWD, highest precision), potentially adjusting the virtual spot size to improve the result.
   (b) If the TW and Wetherill ages are inconsistent, recalculate the ages after averaging the mass scans. If the TW and Wetherill results converge, return to step 3a. If not, the sample is likely undatable.
4. Optional steps:
   - Apply the Rectis method to obtain a potentially more precise age or one with better statistical parameters.
   - Use the sub-image method as an additional test. The weighted mean of the sub-image ages should ideally match the result obtained using the moving grid.

This workflow will be added to the revised manuscript to help users apply our method more effectively and transparently.

- **A number of studies (e.g., van Elteren et al., 2018, Norris et al., 2021) have shown that aliasing and other artefacts can be created by LA-ICP-MS mapping. Have you observed any such effects, how are you mitigating such effects and how would this influence your ages?**

We have not encountered such issues, except for a slight smearing effect related to the washout time, which should have no significant impact on the accuracy of the obtained ages (see also our response to Reviewer 1). However, it is plausible that effects such as aliasing could have a more substantial influence on the calculated isotopic ratios and, consequently, on the ages derived using our approach. This remains to be tested and represents an avenue for future investigation.

Technical Comments:

- **Use of the word 'image' when referring to the laser map, in many cases even using 'image map'. Images imply that pixels are acquired simultaneously, which is not the case for LA-ICP-MS. Therefore, the word map should be used in this case. Please change this throughout the manuscript.**

OK. We will follow these recommendations.

Line 55 & 62: use 238U/208Pb, we were wondering if this is a typo and should say 238U/206Pb.

This is not a typo. The $^{238}U/^{208}Pb$ ratio is used in the approach of Drost et al. (2018). See their paper for additional detail.

Line 76/77: 'Both allowed to obtain highly spatially resolved image maps (25 µm rasters) and with a good analytical sensitivity.' What is good analytical sensitivity in this case, can you please quantify this?

Taking NIST SRM 614 as an example, at 500 Hz, analytical conditions used give about 100 kcps – 200 ckps / ppm ^{238}U depending on the session. These values will be added to the text. Limits of detection and quantification are provided l. 147-148.

- **Line 169: 'This script as well as the ones described below are publicly available (Hoareau et al., 2024).' Instead of saying it is publicly available and referring to another paper it should say where the code is available. Good practice is to publish the code on GitHub and then provide the link here. Make it easy for people to find and use!**

We will ensure that the code made available on Zenodo is cited appropriately, as indicated in the Data Availability section. At this stage, we do not plan to publish the code on GitHub.

- **Line 172 should say virtual spot**

Yes.

- **Inconsistent use of NIST glass names, sometimes NIST SRM 612/614 other times NIST 612/614. We suggest to always use the same labelling.**

OK. We will use NIST SRM 612 and NIST SRM 614.

- **The use of the word spot height is a bit confusing, we suggest using width instead when talking about the vertical extent and then speaking about line length when speaking about the horizontal extent.**

We had the same remark from first reviewer. It will be changed.

- **Line 183-185: "To achieve this, it may be necessary to adjust the size of the virtual spots very slightly (e.g., 51 µm x 50 µm instead of 50 µm x 50 µm) to ensure an integer number of pixels per spot."**

- **Why is it, is it because of the Python language/computing characteristics?**

The user interface allows the user to specify virtual spot sizes in microns. The calculation then divides this length by the chosen mass scan duration to determine the number of pixels, which in turn defines the tolerated offsets between successive moving grids. Slightly adjusting the virtual spot size can result in a greater number of possible grid positions, as it leads to more integer values in the calculations. This behaviour is independent of the programming language used.

- **Fig 1. The use of the arrows from A to B&C is confusing as they are not derived from A. They simply show a different configuration or the grid. Therefore, we suggest deleting the arrows. Furthermore, it would be good to provide the information on what map is shown. Is that a raw map? What element/ratio does it show? What sample is it?**

We agree. We will remove the arrows and add the ratio displayed ($^{238}U/^{206}Pb$). Sample is BH14 as explained in the caption.

- **Fig 2. This figure is quite busy, are all images needed? Could some of them go into the supplement?**

Since the Figure presents the maps used and discussed in the study, we feel that keeping them in the main text is a minimum.

- **In the caption of Fig 2, it says that concentrations were estimated from NIST SRM. First of all, which NIST was used for which sample? And secondly, what do you mean by estimates? Why not do a proper calibration of them?**

Concentrations are semi-quantitative estimates based on analysis of NIST SRM 612 (before 2020) and NIST SRM 614 (after 2020), as calculated from Iolite4. Purely quantitative concentrations would require the analysis either of ^{42}Ca mass or that of a carbonate standard of homogenous U, Th and/or Pb concentration. The term ‘estimates’ can be replaced by ‘semi-quantitative’.

- **Fig. 7: The maps at the top have two areas highlighted that represent two calcite generations. What is the rest of the map? Nowhere does it say what it is and based on what the areas highlighted have been chosen.**

The rest of the map is made of quartz (in blue) and calcite (in red). The highlighted areas have been chosen based in a sufficiently high $^{238}U/^{206}Pb$ for calcite rhombs (area 1) and the presence of a calcite-filled fracture (area 2). We will label the quartz grains and non-analysed calcite, as well as provide more detail in the text.

The virtual spot approach: a simple method for image U-Pb carbonate geochronology by high-repetition rate LA-ICP-MS.

Guilhem Hoareau[1], Fanny Claverie[2], Christophe Pecheyran[2], Gaëlle Barbotin[2], Michael Perk[3], Nicolas E. Beaudoin[1], Brice Lacroix[4], E. Troy Rasbury[5]

[1]Universite de Pau et des Pays de l'Adour, E2S UPPA, CNRS, LFCR, UMR5150, Pau, France
[2]Universite de Pau et des Pays de l'Adour, E2S UPPA, CNRS, IPREM, UMR5254, Pau, France
[3]Institute of Operating Systems and Computer Networks Algorithms, TU Braunschweig, 38106 Braunschweig, Germany
4Department of Geology, Kansas State University, 108 Thompson Hall, Manhattan, KS, 66506
[5]Department of Geosciences, FIRST, Stony Brook University, 100 Nichols Rd, Stony Brook, NY 11794-2100, USA

Correspondence to: Guilhem Hoareau (guilhem.hoareau@univ-pau.fr)

Abstract. We present a simple approach to laser ablation inductively coupled plasma mass spectrometry (LA-ICP-MS) U-Pb dating of carbonate minerals from isotopic image maps, made possible using a high repetition rate femtosecond laser ablation system. The isotopic ratio maps are built from 25-µm-~~height~~width linear scans, at a minimal repetition rate of 100 Hz. The analysis of ^{238}U, ^{232}Th, ^{208}Pb, ^{207}Pb and ^{206}Pb masses by a sector field ICP-MS is set to maximize the number of mass sweeps, and thus of pixels on the produced image maps (~8 to 19 scans s^{-1}). After normalization by sample standard bracketing using the Iolite 4 software, the isotopic ~~image~~ maps are discretized into squares. The squares correspond to virtual spots of chosen dimension, for which the mean and its uncertainty are calculated, allowing to plot corresponding concordia diagrams commonly used to obtain an absolute age. Because the ratios can vary strongly at the pixel scale, the values obtained from the virtual spots display higher uncertainties compared to static spots of similar size. However, their size, and thus the number of virtual spots can be easily adapted. A low size will result in higher uncertainty of individual spots, but their higher number and potentially larger spread along the isochron can result in a more precise age. Reliability of this approach is improved by using a mobile grid for the virtual spot dataset of a set size, returning numerous concordia diagrams allowing to select the more statistically robust result. One can also select from all the possible spot locations on the image map, those that will enable regression to be obtained with the best goodness of fit. We present examples of the virtual spot approach, for which in the most favorable cases (U > 1 ppm, $^{238}U/^{206}Pb >> 1$, and highly variable U/Pb ratios) a valid age can be obtained within reasonable uncertainty (< 5-10%) from maps as small as 100 µm x 100 µm, i.e. the size of a single spot in common in situ approaches. Although the method has been developed on carbonates, it should be applicable to other minerals suited to U-Pb geochronology.

1 Introduction

The in-situ uranium-lead (U-Pb) dating of carbonate minerals (calcite, dolomite) by laser ablation inductively coupled plasma mass spectrometry (LA-ICP-MS) is now a well-established approach (Roberts et al., 2020). Due to the ubiquitous nature of carbonates in the upper crust, and to the sub-millimetre-scale spatial resolution of the method, in situ U-Pb dating has been applied successfully to a variety of geological contexts and objects such as tectonic fractures and veins (e.g. Beaudoin et al., 2018; Nuriel et al., 2019; Roberts and Holdsworth, 2022), carbonate deposition (e.g. Drost et al., 2018; Montano et al., 2021), speleothems (e.g. Woodhead and Petrus, 2019) or cements (e.g. Brigaud et al., 2020; Motte et al., 2021). Aside from the LA-ICP-MS approach used by most laboratories worldwide, which consists in the construction of isochrons from the combination of several tens of ablation craters (80 to 235 µm) made on the same or adjacent crystals, recent studies have demonstrated the feasibility of obtaining carbonate U-Pb ages from isotope ratio maps (Drost et al., 2018; Roberts et al., 2020; Hoareau et al., 2021; Rochín-Bañaga et al., 2021; Davis and Rochín-Bañaga, 2021; Liu et al., 2023). This approach has also successfully been applied to zircon (Chew et al., 2017), apatite (Ansberque et al., 2020; Liu et al., 2023) and monazite (Chew et al., 2021). Its principle is identical to that used to make elemental mineral concentration maps by LA-ICP-MS, i.e. rastering the laser spot along successive (usually horizontal) lines by moving the stage, combined with continuous isotopic mass measurement of the ablation products (e.g., Kosler, 2008). The time-resolved signals obtained for each line are then combined to form the isotopic~~image~~ maps, so as each 'pixel' corresponds to a mass sweep of the spectrometer. In order to account for the washout time of the ablation chamber, which may exceed the duration of a single mass sweep, it is common practice to average several mass sweeps to avoid smearing effects on the produced maps (e.g., Drost et al., 2018; Chew et al., 2021). An obvious advantage of the isotope mapping~~his~~ approach is that it allows both to visualize the distribution of trace elements over the analyzed area, and to obtain an age in the most favourable cases (U and Pb contents typically above 1 ppm, and variable, positive U/Pb ratios) (Drost et al., 2018). As with concentration maps, the analysis of several element masses (in addition to those useful for dating) can identify areas that may correspond to solid inclusions (e.g. clays) or to diagenetic alteration (e.g., Roberts et al., 2020). Filtering-out the corresponding pixels makes it possible to keep only the most favorable zones for dating~~,~~ and thus maximize the chances of obtaining a reliable age from the masses used for U-Pb dating (typically ^{238}U, ^{207}Pb and ^{206}Pb) (Drost et al., 2018; Roberts et al., 2020; Hoareau et al., 2021).

Whereas the analytical conditions used for ~~image~~map-based carbonate dating are quite comparable to those used for "traditional" elemental mapping, the data treatments necessary to calculate an age from isotopic image maps are highly variable among studies published so far, with possible repercussions on the reliability of the ages obtained. The study of Drost et al (2018) showed the potential of the pixel pooling approach, which uses ratios other than those used for dating (^{238}U/^{208}Pb, ^{207}U/^{235}U) to sort the pixel ratio values, split the resulting empirical cumulative distribution function (ECDF) into subsets, and calculate mean ratios and their uncertainty for each subset ("pseudo-ellipses"). This method tends to maximize the spread of the subset ratios along an isochron, ideally resulting in more precise ages. The potential for obtaining accurate and very precise ages even with a quadrupole ICP-MS has also been highlighted by Roberts et al. (2020) and Hoareau et al. (2021). However, as pointed out by the authors, the sorting approach of Drost et al. (2018) cannot be used blindly as it is likely to cause biases in the calculated ages (i.e., precise but inaccurate ages) if the sample is not well characterized and the pixel values filtered adequately. For example, using either ^{238}U/^{208}Pb or ^{207}Pb~~U~~/^{235}U as the sorting ratio may result in two distinct, but statistically plausible ages (i.e., MSWD close to 1). In addition, the calculated common Pb values may be biased (Hoareau et al., 2021). In the latter study, we also presented an alternative approach consisting in running a robust regression through the pixel ratio values in a concordia diagram. In most cases, it allows to obtain ages identical to those of Drost et al. (2018) both in terms of accuracy and precision. However, the approach of Drost et al. (2018) shows better performance in terms of accuracy when the U concentrations of the analyzed samples are low (typically a few hundred ppb). Finally, Davis and Rochín-Bañaga (2021) and Liu et al. (2023) have recently presented another approach, based on the use of Bayesian inference in age calculation. In this approach, it is first better to calculate an age and common Pb range by a classical regression approach (York type) through the pixel ratio values~~s~~ to which uncertainties related to the number of counts have been added. Then, a planar regression in a 3D concentration diagram is used to refine this age by Bayesian statistics. This approach shows great potential and will likely gain major attention in future studies. However, it is likely that the bias in age results reported in some cases by Hoareau et al. (2021) and in the present study may also apply with this approach, since pixel ratio values located far from the discordia line in a concordia diagram, which do not necessarily correspond to clear outliers in time-resolved data, may~~are~~ also be considered in the Bayesian regression.

In their image-based dating methodology, Hoareau et al (2021) used a high repetition rate femtosecond laser (500 Hz), allowing to use a small spot diameter~~width~~ (15 µm), coupled to a high-resolution SF-ICP-MS. Both allowed to obtain highly spatially resolved image maps (25 µm rasters) and with a good analytical sensitivity (100 kcps – 200 ckps / ppm ^{238}U on NIST SRM 614). In addition to the robust regression method that is the ~~main focus~~focus of their work, Hoareau et al (2021) also presented an approach based on a squaring of the image maps, with averaging and uncertainty calculation for each square called "pseudo spot". It was intended to check the accuracy of the ages obtained by the other methods compared (robust regression, and the method of Drost et al. 2018). Note that similar comparison between such map discretization and the pixel pooling approach of Drost et al. (2018) was also recently proposed by Subarkah et al. (2024). In the Hoareau et al. study (2021), ~~this~~ discretization was performed after averaging the number of pixels, which results in uncertainties too high for the obtained ages to be satisfactory for use in geoscience case studies. In the present study, we further develop the image discretization (squaring) approach. On the one hand, we avoid, or limit averaging the number of pixels to maximize the ~~spatial resolution~~number of pixels of the ~~image~~ maps and improve the statistics of the calculated ratios. On the other hand, we propose evolutions allowing to calculate several ages for a single ~~image~~ map, either by moving the grid allowing its discretization into virtual spots, or by creating sub-images within the image. In the latter case, a weighted average of ages obtained at different locations in the image map can be calculated. We show that this approach, which we call here "virtual spots", is well suited to highly spatially resolved images. It can be used to obtain ages comparable to those calculated by classical approaches based on in situ spots, while being flexible and simple in its implementation.

2 Samples

Seven (7) samples of carbonates have been chosen to test the new approach, among which 5 have been previously dated. Among the 7 samples, two (BH14 and C6-265-D5) were previously analyzed as part of the study of Hoareau et al. (2021). The samples are:

(i) a tectonic calcite vein (AUG-B6) from the Paris basin (France) dated by U–Pb LA-ICP-MS spot analyses (i.e. range of spot ablations) at about 42 to 43 Ma in several laboratories (Pagel et al., 2018; Blaise et al., 2023), including ours (42.8 ± 2.0 Ma (2s); MSWD = 3.7; the detailed methodology is presented in the Supplement S1 including Table S1 and Fig. S1). A petrographical description of AUG-B6 is available in Pagel et al. (2018).

(ii) a tectonic calcite vein (BH14) from the Bighorn Basin (Wyoming, USA) dated by U–Pb LA-ICP-MS spot analyses (i.e. range of spot ablations) at 63.0 ± 2.2 Ma (MSWD=1.6) by Beaudoin et al. (2018) and at 61.2 ± 2.9 Ma (MSWD = 4.1) in our laboratory (see Hoareau et al., 2021).

(iii) a dolomite cement (C6-265-D5) found in a tectonic breccia affecting Callovo-oxfordian limestones of the northern Pyrenees (France). It was dated at 106.1 ± 5.5 Ma from U-Pb LA-ICP-MS by the image-based method of Drost et al. (2018) but using WC1 as the primary standard (see Motte et al., 2021, including a petrographical description of the sample as $DC4_{Meillon}$).

(iv) a lacustrine limestone (Long Point; Duff Brown Tank locality in the Colorado Plateau, USA), precisely dated by Hill et al. (2016) at 64.0 ± 0.7 Ma (2s) by U–Pb methods using isotope dilution (ID) multi-collector inductively coupled plasma mass spectrometry (MC-ICP-MS), and labelled DBT in the following. This sample is widely used as a validation RM.

(v) a Tithonian dolostone from the northern Pyrenees (Senz7) which we have precisely dated by ID-MC-ICP-MS at 147.0 ± 2.4 Ma (2s) (see Supplement S2 including Fig. S2 for the detailed methodology). Like C6-265-D5, this sample was also dated in April 2019 to ∼137 Ma (∼7% too young) by the image-based method of Drost et al. (2018), using WC1 as the primary standard (see Motte et al., 2021, including a petrographical description of the sample as $RD1_{Mano}$).

(vi) a calcite-cemented sedimentary breccia (Collings Ranch Conglomerate) from the Arbuckle Mountain (USA). The calcite cement (ARB20-2D) has not been previously dated. The intergranular cement is made of blocky calcite, dull in cathodoluminescence excepted rare grains with concentric zoning defining a second calcite generation (Fig. S3).

(vii) a deformation band affecting a calcarenite (Cot2a) from the Cotiella basin of Cretaceous age in southern Pyrenees, Spain (see Taxopoulou et al., 2023 for a petrographical description). The calcite cements located in the deformation band have not been previously dated.

3 Analytical strategy

All the samples were analyzed with a 257 nm femtosecond laser ablation system (Lambda3, NEXEYA, Bordeaux, France) coupled to a sector field inductively coupled plasma mass spectrometer (SF-ICP-MS) Element XR (Thermo Fisher Scientific, Bremen, Germany) fitted with the Jet Interface, at the IPREM laboratory (Université de Pau et des Pays de l’Adour, Pau, France), in October 2018 (BH14), April 2019 (C6-265-D5), April 2022 (AUG-B6, ARB20-2D, DBT), and May 2023 (Senz7, Cot2a). The analytical conditions are essentially like those previously detailed in Hoareau et al. (2021). Before 2020, polished chips were ablated at a repetition rate of 500 Hz with a fluence of ~2 µJ per pulse, along 23 to 25 linear scans of 0.72 to 1.21 mm ~~wid~~length~~th~~ (Table 1). These lines are 25 µm ~~height~~width, ~~separated by 25 µm so that they are~~ adjacent to each other, and ~~were~~ obtained using a back-and-forth movement of the laser ~~(at 5 mm s^{-1})~~ combined with a stage movement rate of 25 µm s^{-1}. They correspond to 29 to 48.5 s of analysis per linear scan, followed by a 15 s break. After 2020, polished chips or sections (30 or 80 µm-thick) were ablated either at 100 Hz for thin sections (2022), or at 500 Hz for thick sections and polished chips (~~May~~ 2023), with a fluence of ~2~~7~~ µJ per pulse, along 8 to 32 linear scans of 0.72~~96~~ to 3.62 mm ~~width~~length, . ~~The adjacent lines are 25 µm height, with similar laser and stage movement rates than previous sessions, except that~~ and breaks between lines ~~were~~ increased to 25 s. Ablations correspond to 38.3 to 145 s of analysis per linear scan. All sessions considered, the total analysis time was of ~5.5 to 31.3 min for a complete image map of a surface of between 0.19~~45~~ and 1.16 mm^2 (Table 1). The maximum ablation depth is about 25 µm at 100 Hz, and 40 µm at 500 Hz as measured with a digital microscope. Before analysis, all samples were pre-cleaned with the laser using a stage movement rate of 200 µm s^{-1}.

Sample name (alphabetical order)	**Date**	**Line length~~width~~ (mm)**	**Ablation duration per line (s)**	**Number of lines**	**Total analysis time (min)**	**Number of pixels**	**Area (mm^2)**	**Repetition rate (Hz)**	**Dwell time (ms)**
ARB20-2D	03/2022	3.625	145	8	19.7	20488	0.725	100	57
AUG-B6	03/2022	0.957	38.3	8	5.52	5208	0.191	100	57
BH14	10/2018	1.212	48.5	23	18.8	8326	0.697	500	134
C6-265-D5	04/2019	0.722	28.9	25	12.3	10675	0.452	500	68
Cot2a	05/2023	1.450	58.0	32	31.3	33696	1.16	500	57
DBT	03/2022	1.950	78.0	8	10.8	11024	0.390	100	57
Senz7	05/2023	1.237	49.5	8	7.02	7000	0.248	100	57
WC1 / NIST		0.550	22	8	3.35	~3100	0.11	100 / 500	57 / 68/ 134

Table 1: Operating conditions

The aerosol generated by ablation was transported to the ICP-MS using a helium (He) stream at 600 mL min^{-1}, except in October 2018 (BH14) when argon (Ar) was used at 650-700 mL min^{-1}. The washout time for the ablation cell was approximately 500-600 ms for He gas and ~1 s for Ar gas, based on the 99% criterion. To enhance sensitivity, 10 mL min^{-1} of nitrogen was added to the twister spray chamber of the ICP-MS through a tangential inlet, while He was introduced via another tangential inlet located at the top of the spray chamber. All measurements were performed under dry plasma conditions. The femtosecond laser ablation inductively coupled plasma mass spectrometry (fs-LA-ICPMS) setup was tuned daily to optimize sensitivity, accuracy, particle atomization efficiency, and stability. The additional Ar carrier gas flow rate, torch position, and power were adjusted to achieve a U/Th ratio close to 1±0.05 during the ablation of NIST SRM 612 glass. Daily checks were performed for detector cross-calibration and mass bias calibration using the Element software sequence. The laser and ICP-MS parameters for U–Pb dating are detailed in Table A1. The selected isotopes were ^{238}U, ^{232}Th, ^{208}Pb, ^{207}Pb, and ^{206}Pb, resulting in a total mass sweep time of ~57 ms (except for ~139 ms in October 2018 for BH14 and ~68 ms in April 2019 for C6-265-D5). As of May 2023 (500 Hz), the detection limits were approximately 1.1 ppb for ^{206}Pb and 0.02 ppb for ^{238}U, while the quantification limits were about 3.5 ppb for ^{206}Pb and 0.07 ppb for ^{238}U. The unknown samples were bracketed with NIST SRM 612 (before 2020: BH14, C6-265-D5) and NIST SRM 614 (after 2020: ARB20-2D, AUG-B6, Cot2a, DBT, Senz7), as well as the commonly used WC-1 calcite RM (Roberts et al., 2017). Small maps of the primary RMs (~0.1 mm², ~3.5 min of analysis time) were generated before and after each unknown sample analysis under similar conditions. Details on the laser and ICP-MS parameters used for U–Pb dating can be found in Appendix A.

4 Data processing

4.1 Initial data processing in Iolite

U-Pb data were processed as time-resolved signal using Iolite 4 software (Paton et al., 2011) and the VizualAge_UcomPbine Data Reduction Scheme for background correction and normalization (Chew et al. 2014). After line selection and background correction, NIST SRM 614 glass was used as the primary reference material for normalization (mass drift and interelement fractionation) of both Pb/Pb and Pb/U isotope data. Pb/Pb ratios are taken from Woodhead and Hergt (2001), while the ^{206}Pb/^{238}U ratio (0.80612) was calculated from Woodhead and Hergt (2001), Duffin et al. (2013), Jochum et al. (2011), and CIAAW-IUPAC. Correction of additional matrix-related offset of the ^{206}Pb/^{238}U ratio used WC-1 calcite reference material (age 254.4 ± 6.4 Ma), using the method of Roberts et al. (2017). The DBT limestone (Age 64.04 ± 0.67; Hill et al., 2016) was used as validation reference material. The isotopic maps ~~The ratio values for each pixel~~ are obtained in the "Imaging" section of Iolite. ~~–~~ On these maps, what we refer to as a "pixel" corresponds to the surface area covered by the laser during a mass sweep, which is approximately 25 µm x 1.2 µm for a 57 ms mass sweep. This duration is shorter than the washout time of the ablation chamber (~500 ms), resulting in signal mixing between adjacent pixels and thus possible smearing of the maps. Although the high number of pixels resulting from short mass sweeps may offer statistical advantages for the virtual spot approach as explained below, it does not imply better spatial resolution as the latter is limited by the washout time. Nevertheless, Iolite 4~~The software~~ allows the operator to filter out pixels that are considered anomalous, like the Monocle plugin of the previous Iolite version. Here, only pixels with negative ratio values were excluded, except for sample AUG-B6. For the latter, the presence of numerous spikes on the ^{207}Pb/^{206}Pb ratios result in expected age values but very high common lead values (0.85-0.9) in Tera-Wasserburg (TW) concordia diagrams. To obtain values closer to those expected (0.8-0.85), pixels with ^{207}Pb/^{206}Pb values higher than 1.5 were removed.

4.2 Python API processing

An in-house Python script was then used as part of the Python API embedded in Iolite 4. This script as well as the ones described below are publicly available in a Zenodo repository (Hoareau et al., 2024; see Data availability section). The Python script allows to reconstruct isotopic ratio matrices from pixel values, to add excess variance to individual ratio uncertainties, to correct of matrix-related offset of the ^{206}Pb/^{238}U ratio, to split the isotopic image maps into virtual spots forming a grid, and to calculate the mean and its uncertainty for each virtual spot, for all ratios. First, for each virtual spot the mean of ratios is calculated, pixels identified as outliers, if any, are removed (i.e, pixel ratio values outside the 95% confidence interval of the standard error), and the mean recalculated. Second, excess variance calculated by Iolite 4 based on Paton et al. (2010) using all ablation lines of NIST SRM 614 (typically 1.5-2.5% (2s) for ^{238}U/^{206}Pb and 0.1-0.3 (2s) for ^{207}Pb/^{206}Pb) is added by quadrature to the uncertainties of each virtual spot obtained from the unknowns (and WC-1) within the session. For correction of the matrix-related offset, the isotopic image of WC-1 produced from all lines obtained in the analytical session is split in virtual spots of size like those used on the unknowns. The mean and uncertainty values of ^{238}U/^{206}Pb and ^{207}Pb/^{206}Pb ratios are then plotted in TW diagrams using IsoplotR (Vermeesch, 2018) to calculate its age used for correction. After these first steps, virtual spots are calculated for the unknowns. Whereas their minimum ~~height (~~vertical size~~)~~ is limited to the width of ~~that~~ a line (25 µm), their minimum ~~width (~~horizontal size~~)~~ can theoretically be as small as that of a few microns (few pixels). In that case, the number of virtual spots can exceed several hundreds, resulting in unreasonably high computing times when it comes to age calculation using IsoplotR. In that case, Isoplot (Ludwig, 2003) can be used instead. The script also allows to displace the grid on the matrix, so that new spatial distributions of the virtual spots are obtained (Fig. 1). To achieve this, it may be necessary to adjust the size of the virtual spots very slightly (e.g., 51 µm x 50 µm instead of 50 µm x 50 µm) to ensure an integer number of pixels per spot. Finally, virtual spots with high individual uncertainties can be filtered out.

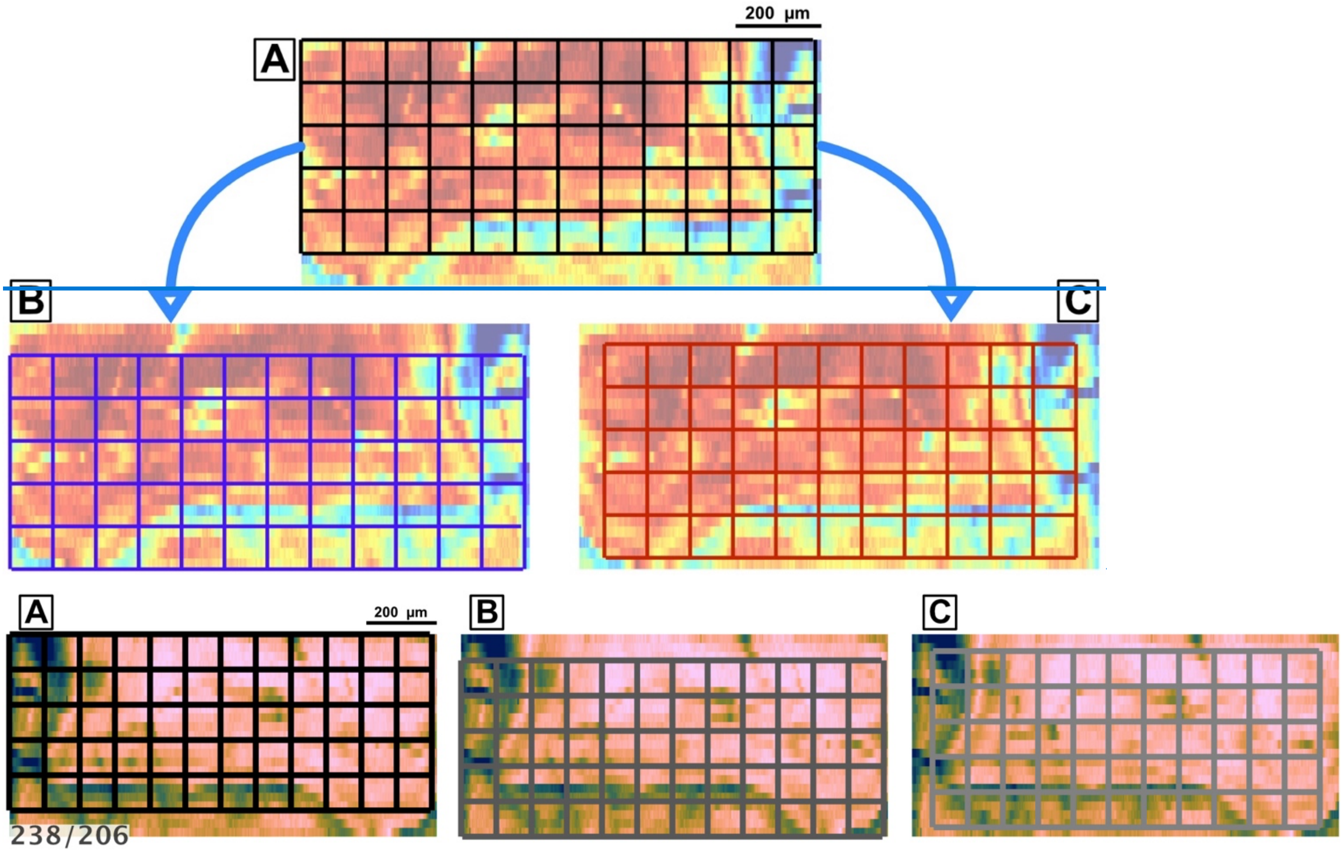

Figure 1: Principle of image map discretization (based on BH14). A: In its default position, the grid defines 60 squares (corresponding to 60 virtual spots). The bottom and the right part of the image map are not considered, as the squares are not complete. B: Example of another grid position, still defining 60 squares. C: Another position where more squares are incomplete and therefore ignored, reducing the total number of squares to 55.

4.3 Age calculation using Python / R

Ages are calculated either from $^{238}U/^{206}Pb$ and $^{207}Pb/^{206}Pb$ (TW) or $^{206}Pb/^{238}U$ and $^{207}Pb/^{235}Pb$ ratios (Wetherill, labelled Weconcordia), and corresponding diagrams generated with an R script using the *age* and *concordia* functions of IsoplotR library. Systematic uncertainties are then added quadratically to the final age. They comprise the decay constant uncertainty of ^{238}U (0.1 %, 2 s), the $^{238}U/^{206}Pb$ ratio uncertainty of WC1, as estimated by Roberts et al. (2017) (2.7 %, 2 s), and the long-term excess variance taken as 2.0 % (2 s). Three types of processing are proposed to obtain ages from the image maps:

(i) First, for a single sample, the ability to change the grid location makes it possible to calculate several dozens of ages corresponding to each grid location (‘mobile grid’ method). This process allows to assess the homogeneity of the sample in terms of age by using weighted mean statistics, and to select the best age obtained in terms of precision and statistical robustness (MSWD value and p). This is the reference processing method that must be systematically used.

(ii) A second algorithm has been developed to calculate the best possible regression in terms of statistical robustness. An orthogonal regression is first performed in a concordia diagram (TW or W) using the values obtained for all the virtual spots that can be defined on the image map (several thousand). The spots can therefore be largely overlapping in space. For a good quality sample, all the values are expected to define a robust linear trend in the concordia diagram, defined by MSWD values close to unity. The regression uses Scipy's ODR function, whose slope and intercept results are strictly identical to a York-type regression. If the age is like those obtained by the first method (mobile grid), the *n* points with a minimum orthogonal distance to the regression can be~~are~~ selected (n = 1000 for example). The corresponding virtual spots can still largely overlap. Finding the largest set of non-overlapping rectangles can be formulated as an independent set problem that uses Boolean variables $\boldsymbol{x_i}$ for every rectangle (Equation 1):

$$max \sum_{x_i} x_i \qquad (1)$$

$$\text{s.t.} \quad \overline{x_i} \vee \overline{x_j} \quad \forall \text{ intersecting } \textit{rectangles} \text{ i, j}$$

$$\boldsymbol{x_i} \in \{\boldsymbol{0}, \boldsymbol{1}\}$$

The constraint programming solver (CP-SAT) is used to solve the model and find the maximum number of non-overlapping virtual spots in the image map. A unique age is then calculated using IsoplotR. Very good goodness-of-fit (GoF) parameters (MSWD, p) are expected. The method is labelled ‘Rectis’ method in the following. It may be used as a complement to the ‘mobile grid’ method.

(iii) The last processing method (‘sub-~~image’~~ map’ method) can calculate a set of ages obtained from creating sub-maps~~images~~ within the isotopic ~~image~~ map. In detail, virtual spots of small size (for example, 25 µm x 25 µm) are first created in Iolite. Then, the isotopic ~~image~~map is splitted in sub-maps~~image~~s of chosen dimension (for example 100 µm x 100 µm). For each sub-~~image~~map, an age is calculated from the virtual spots it contains (i.e., 16 spots of 25 µm x 25 µm for a 100 µm x 100 µm ~~image~~map, or 64 spots for a 200 µm x 200 µm ~~image~~map). As presented in the following, provided samples are suitable, this approach allows to calculate a weighted average of ages obtained at different locations in the ~~image~~ map. It also theoretically makes it possible to obtain reliable ages from ~~image~~ maps of very limited area, and with extremely short analysis times (~ 1.3 to 3 min without the standards). The ‘sub-map’ may also be used as a complement to the ‘mobile grid’ method.

5 Results

The mean U, Pb, and Th concentrations of studied samples, and their $^{238}U/^{206}Pb$ and $^{207}Pb/^{206}Pb$ ratios, are summarized in Table 2. Corresponding ~~image~~ maps are presented in Fig. 2.

Sample name	Reference age (Ma)	U (ppm)	Unc. (2SD)	Pb (ppm)	Unc. (2SD)	Th (ppm)	Unc. (2SD)	$^{238}U/^{206}Pb$	Unc. (2SD)	$^{207}Pb/^{206}Pb$	Unc. (2SD)

ARB20-2D	NA	0.733	0.075	0.22	0.05	0.0011	0.0010	6.71	0.75	0.558	0.031
AUG-B6	~42.5 ± 1.0[1]	4.70	1.50	0.30	0.29	0.028	0.069	43.3	16.5	0.66	0.10
BH14	63.0 ± 2.2[2]	10.7	9.4	0.27	0.10	0.008	0.017	51.4	26.1	0.40	0.17
C6-265-D5	~106.1 ± 5.5[3,*]	0.28	0.22	0.059	0.045	0.064	0.051	19.2	40.5	0.60	0.14
Cot2a	NA	1.27	0.93	14	13	2.4	1.8	1.01	1.11	0.832	0.021
DBT	64.0 ± 0.7[4]	27	3.8	0.81	0.63	0.0295	0.0055	46.5	15	0.40	0.15
Senz7	147.0 ± 2.4[5]	6.5	1.6	0.22	0.12	0.338	0.048	31.3	3	0.256	0.042

Table 2: Mean U, Pb, Th concentrations, and $^{238}U/^{206}Pb$ and $^{207}Pb/^{206}Pb$ ratios of studied samples, as calculated by Iolite4 from raster lines. [1]Pagel et al. (2018) and Blaise et al. (2023). [2]Beaudoin et al. (2018), [3]Motte et al. (2021), [4]Hill et al. (2016), [5]This study. *Not corrected from bias due to the use of a calcite primary standard.

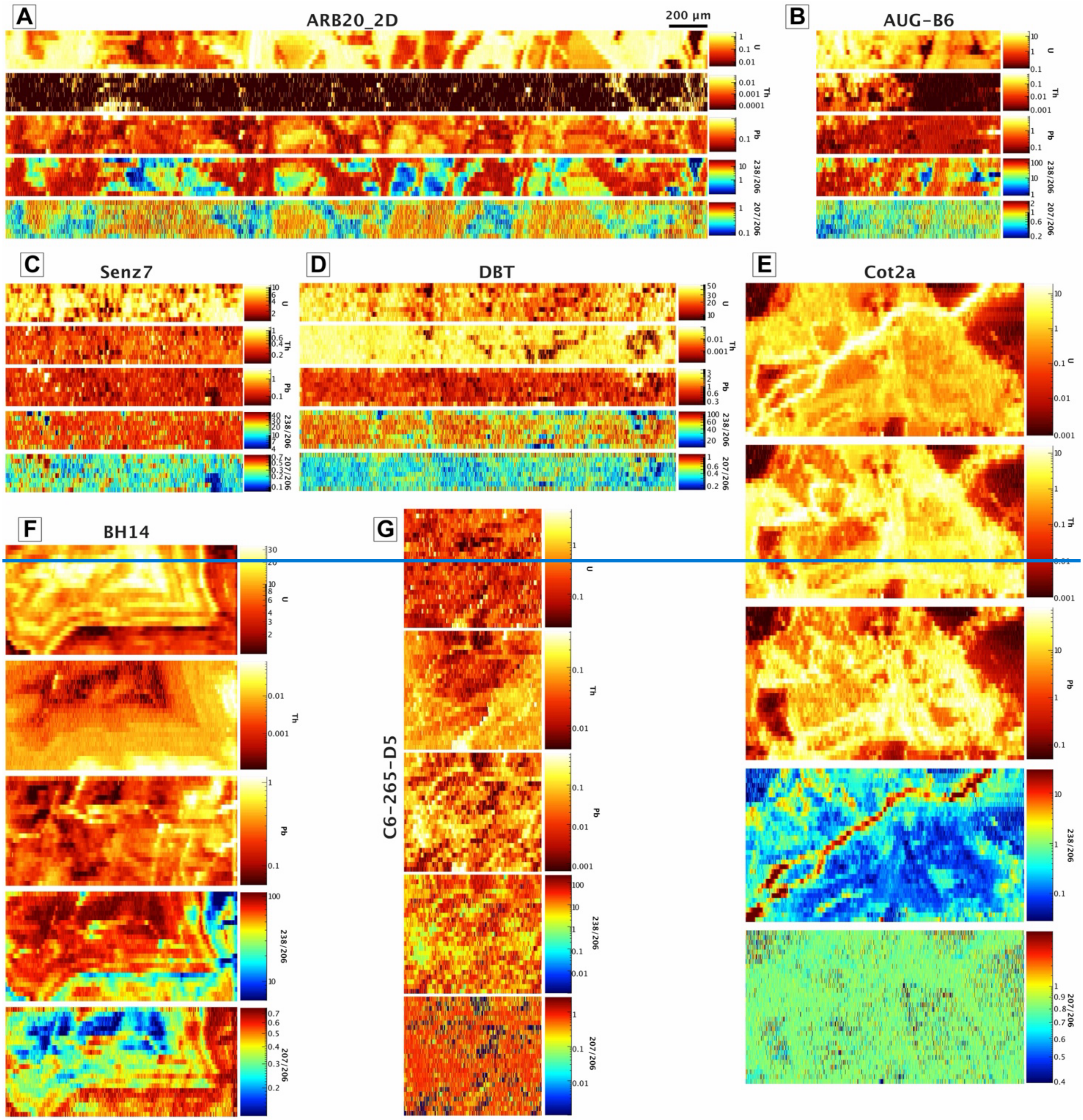

A
ARB20_2D
200 µm
B
AUG-B6
C
Senz7
D
DBT
E
Cot2a
F
BH14
G
C6-265-D5
U
Th
Pb
238/206
207/206

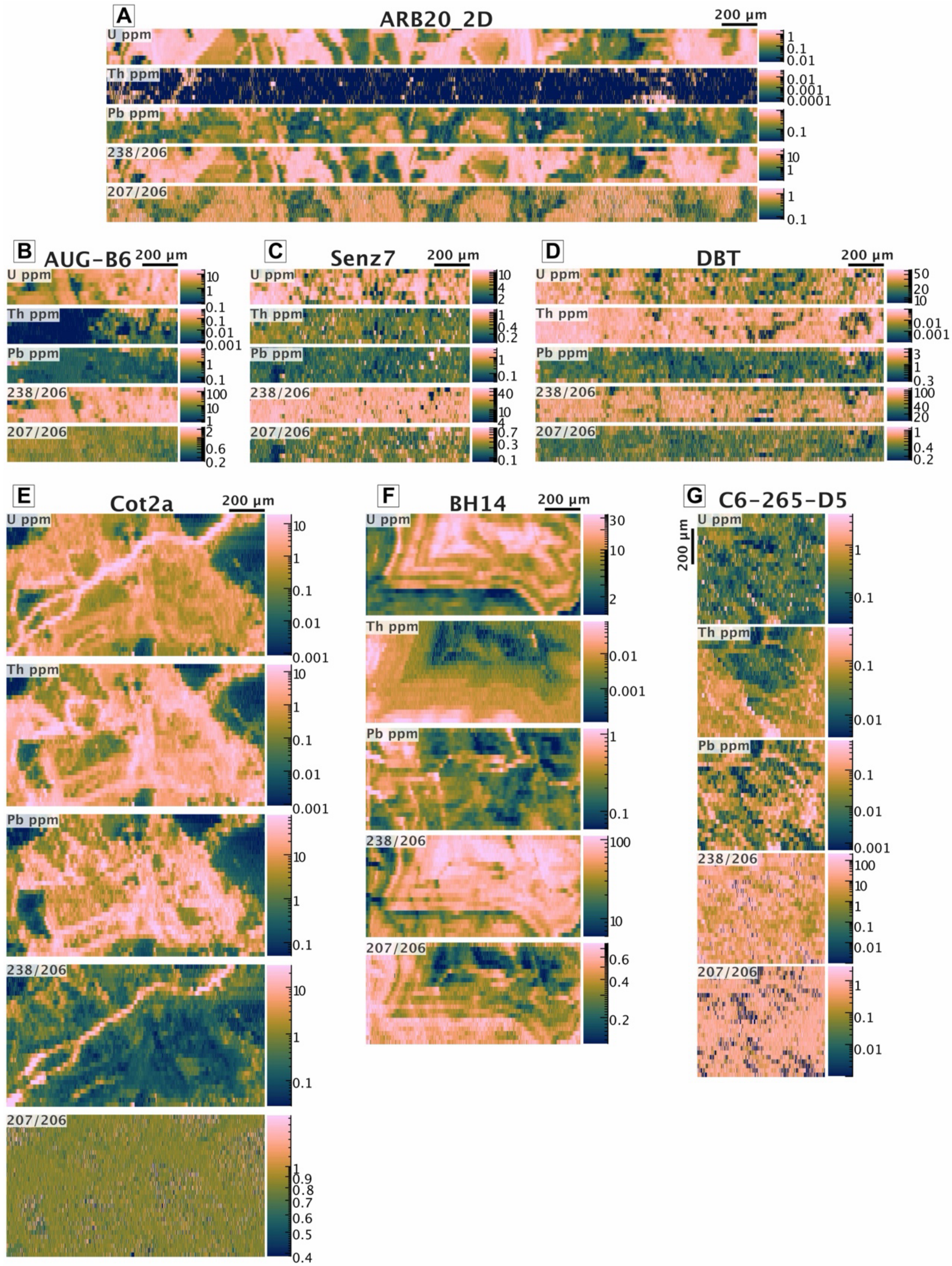

Figure 2: LA-ICP-MS image maps of U, Pb, Th concentrations (in ppm), and $^{238}U/^{206}Pb$ and $^{207}Pb/^{206}Pb$ ratios of studied samples. All maps are at the same scale. Note that concentrations are estimated calculated from NIST SRM 612 (before 2020) or 614 and thus semi-quantitative, and $^{238}U/^{206}Pb$ ratios are not corrected from carbonate RMs.

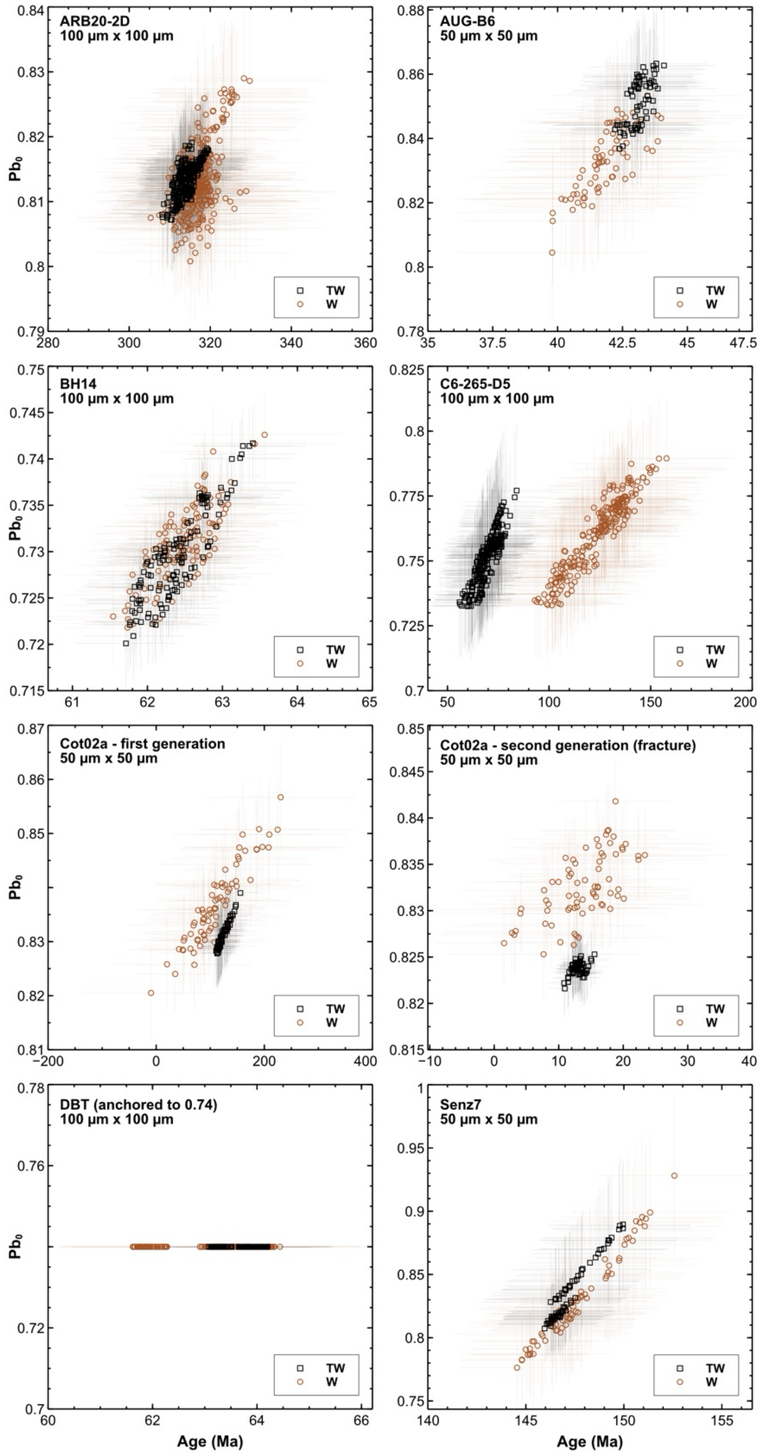

Figure 3: Diagrams showing the ages and common Pb values calculated using the 'moving-grid' method, based on TW (in black) and W (in brown) regressions, for all samples. For each sample, the results from all grid positions are shown. The error bars are at 95% confidence level.

5.1 Examples of ages calculated with mobile grids of different virtual spot sizes

5.1.1 Case of high-U samples

We present ages calculated with different virtual spot sizes for ARB20-2D, AUG-B6, BH14, DBT, and Senz7, which gave satisfactory results owing to high U and Pb contents (Table 2). For samples of age already determined by other studies (AUG-B6, BH14, DBT, Senz7), and using default virtual spot sizes of 100 µm (ARB20-2D, BH14, DBT) or 50 µm (AUG-B6, Senz7) depending on the dimensions of the isotopic maps (Table 1), the ages ~~and common Pb values~~ obtained ~~here~~ are identical to the reference ~~ones~~ ages within uncertainties, ~~whatever~~ regardless of the concordia diagram used (Fig. 3). In detail, common Pb values may show slight variations between TW and W diagrams but remain within uncertainty margins. Overall, TW diagrams always yield more precise results for both age and common Pb values, as indicated by lower individual uncertainties and tighter clustering of data points (Fig. 3). When using TW diagrams as the reference and varying ~~the size of~~ the virtual spot sizes~~s~~ from 200 µm x 200 µm to 25 µm x 25 µm, the resulting ~~chosen~~ ages and common Pb values remain in agreement with expected values (Table 3; Fig. 4~~3~~). In addition, m~~M~~oving the grid over the ~~image~~ maps enables to select the best results from among the different ages calculated for a given spot size (Table 3; Figs~~.~~ 4 and 5~~3~~). For the previously undated sample ARB20-2D, age and common Pb values of ~305-320 Ma and ~0.82 are obtained, respectively. A Pennsylvanian age is fully consistent with the inferred age of deposition of the host conglomerates (Ham, 1954), suggesting their very early cementation. These satisfactory results agree with the good linear distribution of pixel values in a Tera-Wasserburg plot for most samples (Fig. S4). When the default grid is selected (i.e., covering the entire ~~image~~ map surface and therefore with a maximum number of virtual spots), age uncertainty decreases with decreasing virtual spot size (Table 3). This is due to the larger number of virtual spots and their larger spread along the isochron, despite a larger individual uncertainty for each spot, as detailed by Kylander-Klark (2020) and Roberts et al. (2020) based on conventional spot analyses. Selecting the best results puts an end to such correlation, as low age uncertainties can be obtained even for a small number of spots (Table 3; Figs 4 and 5). In the extreme case of spots as low as 25 µm x 25 µm, the resulting age uncertainty can be below 2% (without propagation of external uncertainty). Most samples also display MSWD values higher than 1 that increase with the size of the virtual spots, due to lower individual uncertainties. On the one hand, these values indicate some heterogeneity of the samples, also visible on the TW diagrams (Figs 4~~3~~ and 5~~4~~). Such heterogeneity is, for example, also visible in the conventional spot analyses carried out in the laboratory for samples BH14 and AUG-B6 (Fig. S1 and Fig. 3 of Hoareau et al. (2021)). On the other hand, they are increased by the large error correlation between ratios that the virtual spot approach generates for the most favourable samples (here BH14 and ARB20-2D), as discussed in part 6.1.

Sample name	Virtual spot size (µm)	Grid in its default location (maximum number of virtual spots)				Best results selected from multiple grid locations			
		Number of virtual spots	Age (without/with systematic uncertainty) (Ma)	Pb0	MSWD	Number of virtual spots	Age (without/with systematic uncertainty) (Ma)	Pb0	MSWD
ARB20-2D	200 x 200	18	314.7 ± 15.8 / 18.8	0.815 ± 0.0190	4.8	17	319.9 ± 12.3 / 16.2	0.816 ± 0.01(47	2.4
	150 x 150	24	317.9 ± 16.0 / 19.1	0.818 ± 0.0211	4.3	23	318.3 ± 14.1 / 17.5	0.820 ± 0.0180	3.5
	100 x 100	72	312.4 ± 7.5 / 12.7	0.813 ± 0.0101	2.7	70	313.1 ± 6.7 / 12.3	0.813 ± 0.00988	1.9
	75 x 75	94	310.3 ± 7.4 / 12.6	0.809 ± 0.01106	2.4	92	311.8 ± 6.2 / 12.0	0.813 ± 0.00988	1.8
	50 x 50	284	311.4 ± 4.1 / 11.0	0.816 ± 0.0062	1.4	284	311.4 ± 4.1 / 11.0	0.816 ± 0.0062	1.4
	25 x 25	1136	305.7 ± 3.3 / 10.8	0.817 ± 0.0054	1.4				
AUG-B6	150 x 150	6	45.5 ± 3.2 / 3.5	0.865 ± 0.026	0.6	6	45.5 ± 3.2 / 3.5	0.865 ± 0.026	0.6
	100 x 100	18	44.2 ± 2.2 / 2.6	0.861 ± 0.019	1.1	18	44.2 ± 2.2 / 2.6	0.861 ± 0.019	1.1
	75 x 75	24	41.2 ± 2.8 / 3.1	0.842 ± 0.024	1.7	11	42.4 ± 2.6 / 3.0	0.872 ± 0.022	0.94
	50 x 50	72	42.0 ± 2.1 / 2.5	0.853 ± 0.020	1.7	54	42.4 ± 1.7 / 2.2	0.860 ± 0.017	1.2
	25 x 25	296	41.1 ± 1.5 / 2.0	0.859 ± 0.016	1.4				
BH14	200 x 200	12	61.8 ± 1.7 / 2.7	0.735 ± 0.0203	8.6	5	61.4 ± 0.5 / 2.1	0.727 ± 0.00769	1.1
	150 x 150	24	62.1 ± 1.0 / 2.3	0.732 ± 0.0124	5.3	14	62.0 ± 0.4 / 2.1	0.729	1.2
	100 x 100	60	62.5 ± 0.7 / 2.2	0.734 ± 0.00986	4.7	44	61.6 ± 0.6 / 2.1	0.722 ± 0.0073	2.4

	75 x 75	112	62.0 ± 0.6 / 2.2	0.730 ± 0.007~~1~~	4.6	90	62.1 ± 0.5 / 2.1	0.729 ± 0.006	2.5
	50 x 50	242	62.4 ± 0.5 / 2.2	0.738 ± 0.0054	3.6	230	62.1 ± 0.4 / 2.1	0.732 ± 0.005~~1~~	2.9
	25 x 25	1173	62.3 ± 0.3 / 2.1	0.738 ± 0.0034	2.1				
C6-265-D5	200 x 200	9	82.0 ± 25.0 / 25.1	0.781 ± 0.034	2.4	6	45.0 ± 15.0 / 15.1	0.722 ± 0.029	2.0
	150 x 150	16	68.0 ± 30.0 / 30.1	0.745 ± 0.024	6.6	9	57.0 ± 15.0 / 15.1	0.743 ± 0.031	2.0
	100 x 100	42	76.3 ± 17.1 / 17.3	0.760 ± 0.020	3.7	30	66.1 ± 13.1 / 13.3	0.748 ± 0.026	1.6
	75 x 75	72	75.0 ± 12.0 / 12.3	0.746 ± 0.015	3.0	64	76.0 ± 11.3 / 11.6	0.756 ± 0.016	2.6
	50 x 50	168	75.6 ± 9.7 / 10.0	0.738 ± 0.013	2.4	154	76.2 ± 8.5 / 8.9	0.747 ± 0.014	1.9
	25 x 25	678	76.8 ± 5.9 / 6.4	0.733 ± 0.009	2.0				
Cot2a (late fracture)	200 x 200	12	16.6 ± 6.6 / 6.6	0.827 ± 0.0061	0.8~~76~~	9	14.0 ± 6.1 / 6.1	0.825 ± 0.006~~57~~	0.44
	150 x 150	18	15.1 ± 3.7 / 3.7	0.825 ± 0.0041	1.2	18	15.1 ± 3.7 / 3.7	0.825 ± 0.004~~1~~	1.2
	100 x 100	31	14.1 ± 2.8 / 2.8	0.824 ± 0.0037	1.2	30	11.6 ± 1.8 / 1.8	0.824 ± 0.0~~.~~31	0.84
	75 x 75	46	14.1 ± 2.9 / 2.9	0.825 ± 0.0035	1.2	42	12.9 ± 2.6 / 2.6	0.823 ± 0.0034	0.9~~2~~
	50 x 50	84	13.5 ± 2.3 / 2.3	0.823 ± 0.0036	1.3	79	13.5 ± 1.9 / 1.9	0.825 ± 0.003~~1~~	1.2
	25 x 25	240	12.7 ± 1.5 / 1.6	0.823 ± 0.0032	1.4				
DBT (anchored to 0.740)	200 x 200	9	62.9 ± 2.0 / 2.9	0.740	3.0	8	63.5 ± 1.0 / 2.3	0.740	0.8
	150 x 150	13	63.0 ± 0.9 / 2.3	0.740	1.0	13	63.0 ± 0.9 / 2.3	0.740	1.0
	100 x 100	38	63.1 ± 0.9 / 2.3	0.740	1.7	36	63.0 ± 0.7 / 2.2	0.740	1.3

	75 x 75	50	63.2 ± 0.9 / 1.9	0.740	1.7	48	63.2 ± 0.7 / 2.2	0.740	1.0
	50 x 50	152	63.0 ± 0.6 / 2.2	0.740	1.4	148	63.0 ± 0.6 / 2.2	0.740	1.3
	25 x 25	608	62.5 ± 0.5 / 2.1	0.740	1.4				
Senz7 (self corrected)[a]	200 x 200	6	152.6 ± 12.9 / 13.9	0.940 ± 0.250	0.8~~0~~	6	152.6 ± 12.9 / 13.9	0.94 ± 0.25	0.8~~0~~
	150 x 150	8	156.4 ± 9.2 / 10.6	1.030 ± 0.210	0.4~~36~~	7	153.2 ± 8.1 / 9.6	0.98 ± 0.16	0.4~~36~~
	100 x 100	24	153.4 ± 4.7 / 6.9	0.967 ± 0.093	0.9~~87~~	22	146.3 ± 3.8 / 6.2	0.826 ± 0.051	0.5~~3~~
	75 x 75	32	147.4 ± 3.2 / 5.8	0.840 ± 0.047	1.0	30	145.8 ± 3.2 / 5.8	0.809 ± 0.040	1.1
	50 x 50	96	147.0 ± 2.1 / 5.3	0.821 ± 0.029	1.1	92	146.0 ± 2.0 / 5.2	0.811 ± 0.027	1.2
	25 x 25[b]	384	147.3 ± 1.8 / 5.1	0.823 ± 0.027	1.6				

Table 3: Age and common Pb values obtained with the mobile grid method, for different virtual spot sizes, using the TW regression. The results presented are those obtained with the default grid position, and those corresponding to the best results in terms of precision and MSWD. [a]based on 50 µm x 50 µm virtual spots; [b]One ellipse removed

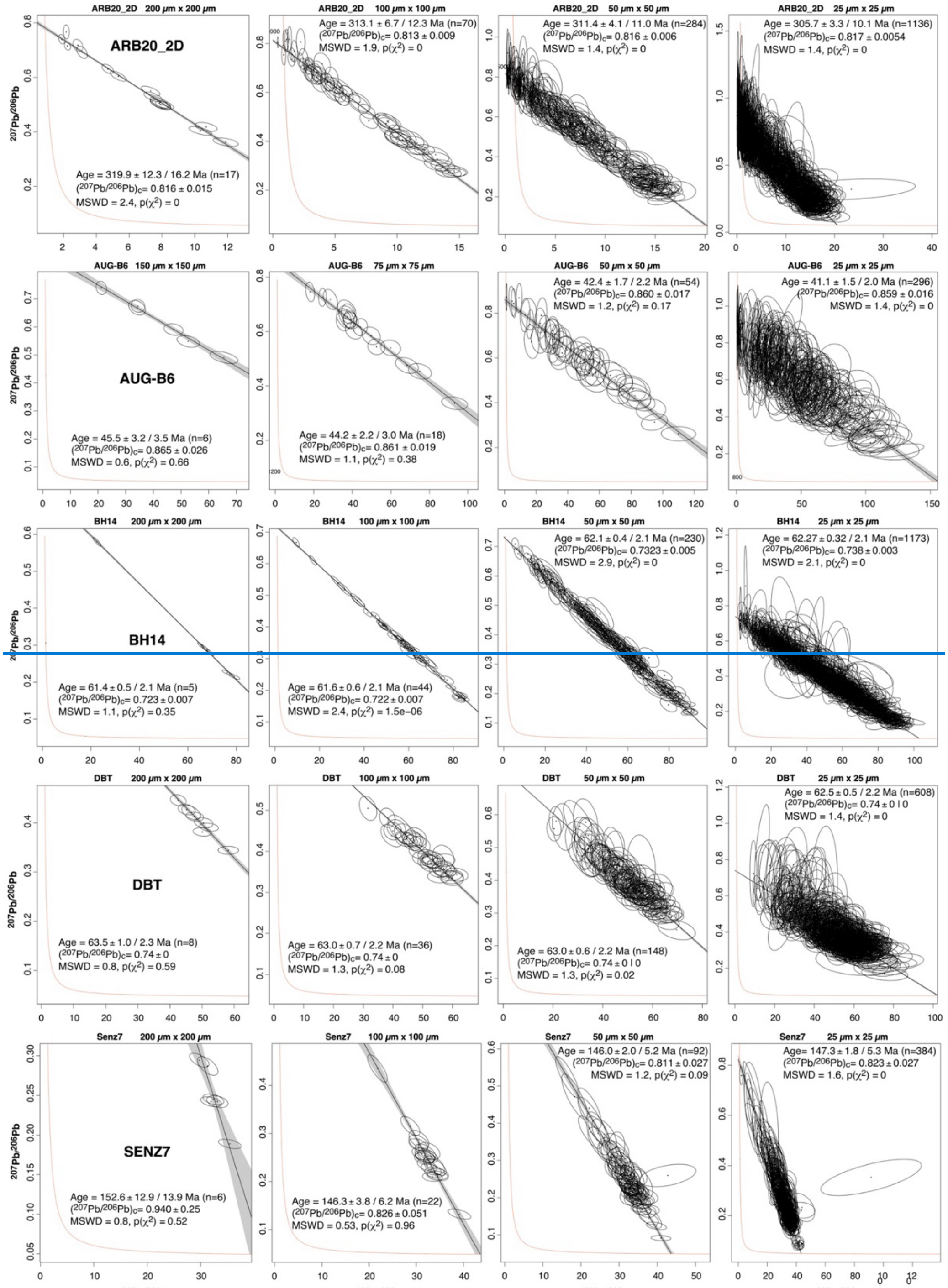

ARB20_2D 200 μm x 200 μm
ARB20_2D
Age = 319.9 ± 12.3 / 16.2 Ma (n=17)
(207Pb/206Pb)c= 0.816 ± 0.015
MSWD = 2.4, p(χ2) = 0
ARB20_2D 100 μm x 100 μm
Age = 313.1 ± 6.7 / 12.3 Ma (n=70)
(207Pb/206Pb)c= 0.813 ± 0.009
MSWD = 1.9, p(χ2) = 0
ARB20_2D 50 μm x 50 μm
Age = 311.4 ± 4.1 / 11.0 Ma (n=284)
(207Pb/206Pb)c= 0.816 ± 0.006
MSWD = 1.4, p(χ2) = 0
ARB20_2D 25 μm x 25 μm
Age = 305.7 ± 3.3 / 10.1 Ma (n=1136)
(207Pb/206Pb)c= 0.817 ± 0.0054
MSWD = 1.4, p(χ2) = 0
AUG-B6 150 μm x 150 μm
AUG-B6
Age = 45.5 ± 3.2 / 3.5 Ma (n=6)
(207Pb/206Pb)c= 0.865 ± 0.026
MSWD = 0.6, p(χ2) = 0.66
AUG-B6 75 μm x 75 μm
Age = 44.2 ± 2.2 / 3.0 Ma (n=18)
(207Pb/206Pb)c= 0.861 ± 0.019
MSWD = 1.1, p(χ2) = 0.38
AUG-B6 50 μm x 50 μm
Age = 42.4 ± 1.7 / 2.2 Ma (n=54)
(207Pb/206Pb)c= 0.860 ± 0.017
MSWD = 1.2, p(χ2) = 0.17
AUG-B6 25 μm x 25 μm
Age = 41.1 ± 1.5 / 2.0 Ma (n=296)
(207Pb/206Pb)c= 0.859 ± 0.016
MSWD = 1.4, p(χ2) = 0
BH14 200 μm x 200 μm
BH14
Age = 61.4 ± 0.5 / 2.1 Ma (n=5)
(207Pb/206Pb)c= 0.723 ± 0.007
MSWD = 1.1, p(χ2) = 0.35
BH14 100 μm x 100 μm
Age = 61.6 ± 0.6 / 2.1 Ma (n=44)
(207Pb/206Pb)c= 0.722 ± 0.007
MSWD = 2.4, p(χ2) = 1.5e−06
BH14 50 μm x 50 μm
Age = 62.1 ± 0.4 / 2.1 Ma (n=230)
(207Pb/206Pb)c= 0.7323 ± 0.005
MSWD = 2.9, p(χ2) = 0
BH14 25 μm x 25 μm
Age = 62.27 ± 0.32 / 2.1 Ma (n=1173)
(207Pb/206Pb)c= 0.738 ± 0.003
MSWD = 2.1, p(χ2) = 0
DBT 200 μm x 200 μm
DBT
Age = 63.5 ± 1.0 / 2.3 Ma (n=8)
(207Pb/206Pb)c= 0.74 ± 0
MSWD = 0.8, p(χ2) = 0.59
DBT 100 μm x 100 μm
Age = 63.0 ± 0.7 / 2.2 Ma (n=36)
(207Pb/206Pb)c= 0.74 ± 0
MSWD = 1.3, p(χ2) = 0.08
DBT 50 μm x 50 μm
Age = 63.0 ± 0.6 / 2.2 Ma (n=148)
(207Pb/206Pb)c= 0.74 ± 0 | 0
MSWD = 1.3, p(χ2) = 0.02
DBT 25 μm x 25 μm
Age = 62.5 ± 0.5 / 2.2 Ma (n=608)
(207Pb/206Pb)c= 0.74 ± 0 | 0
MSWD = 1.4, p(χ2) = 0
Senz7 200 μm x 200 μm
SENZ7
Age = 152.6 ± 12.9 / 13.9 Ma (n=6)
(207Pb/206Pb)c= 0.940 ± 0.25
MSWD = 0.8, p(χ2) = 0.52
Senz7 100 μm x 100 μm
Age = 146.3 ± 3.8 / 6.2 Ma (n=22)
(207Pb/206Pb)c= 0.826 ± 0.051
MSWD = 0.53, p(χ2) = 0.96
Senz7 50 μm x 50 μm
Age = 146.0 ± 2.0 / 5.2 Ma (n=92)
(207Pb/206Pb)c= 0.811 ± 0.027
MSWD = 1.2, p(χ2) = 0.09
Senz7 25 μm x 25 μm
Age= 147.3 ± 1.8 / 5.3 Ma (n=384)
(207Pb/206Pb)c= 0.823 ± 0.027
MSWD = 1.6, p(χ2) = 0
207Pb/206Pb
238U/206Pb

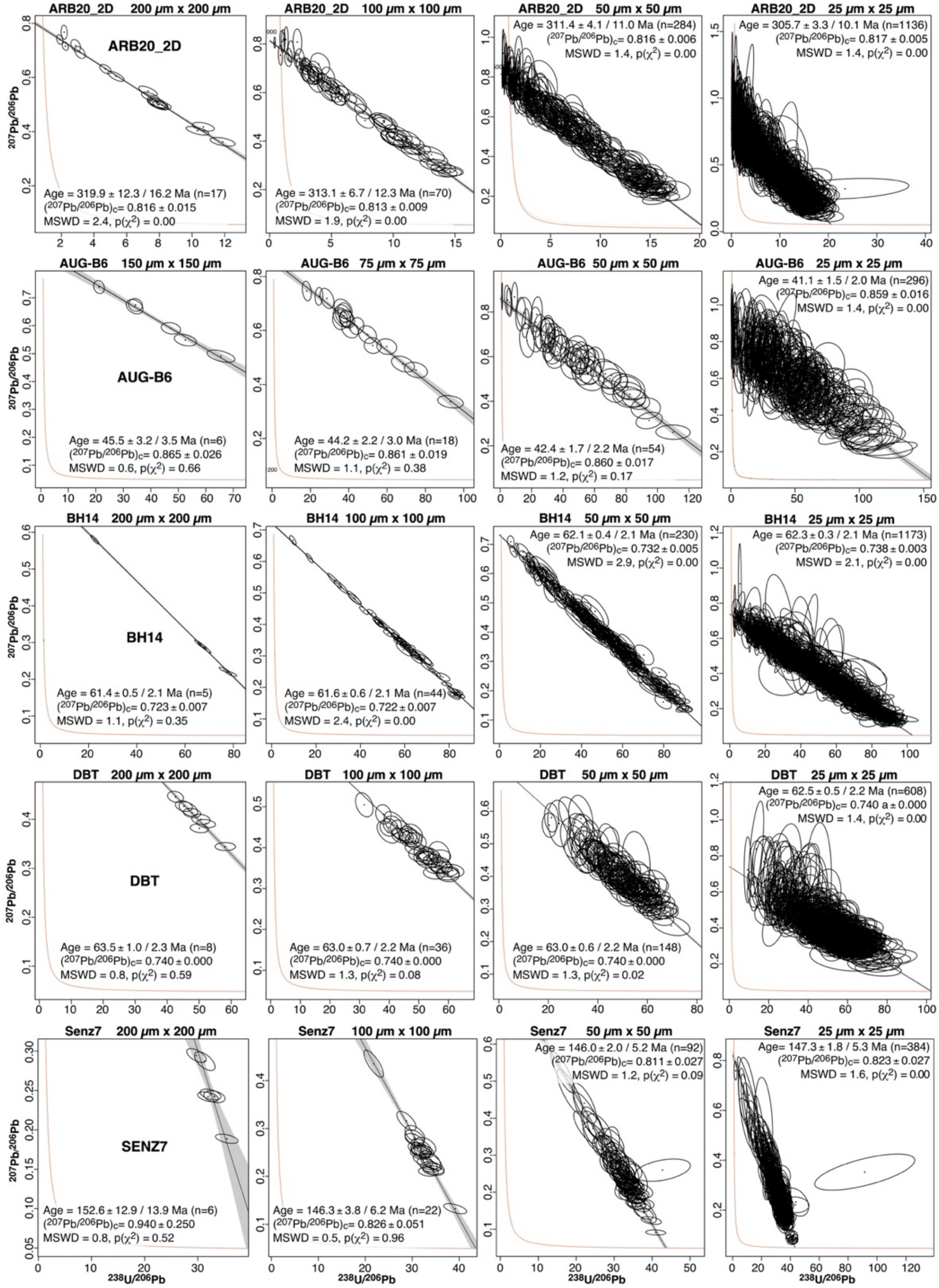

Figure 43: TWTera-Wasserburg diagrams obtained for 5 samples (ARB20-2D, AUB-B6, BH14, DBT, Senz7 from top to bottom) for spot sizes of 200 µm x 200 µm, 100 µm x 100 µm, 50 µm x 50 µm and 25 µm x 25 µm (except sample AUG-B6: 150 µm x 150 µm, 75 µm x 75 µm, 50 µm x 50 µm and 25 µm x 25 µm). The diagrams correspond to the grid positions giving the best results in terms of precision and MSWD.

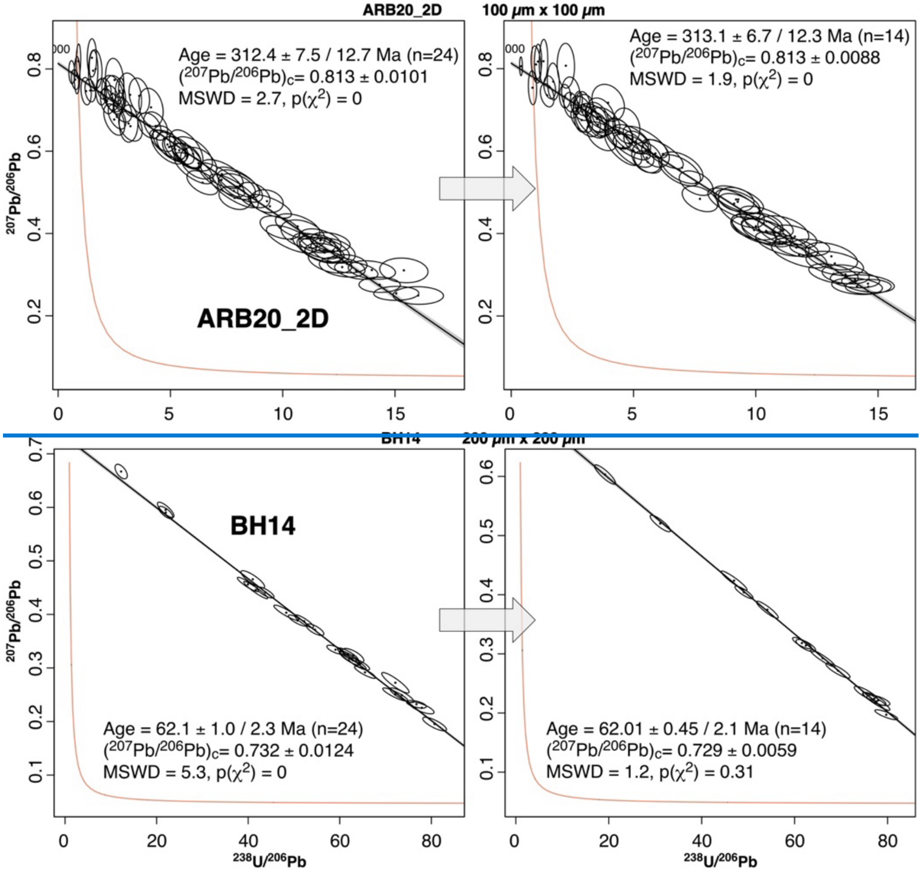
ARB20_2D
100 μm x 100 μm
Age = 312.4 ± 7.5 / 12.7 Ma (n=24)
(207Pb/206Pb)c= 0.813 ± 0.0101
MSWD = 2.7, p(χ2) = 0
ARB20_2D
Age = 313.1 ± 6.7 / 12.3 Ma (n=14)
(207Pb/206Pb)c= 0.813 ± 0.0088
MSWD = 1.9, p(χ2) = 0
207Pb/206Pb
BH14
200 μm x 200 μm
BH14
Age = 62.1 ± 1.0 / 2.3 Ma (n=24)
(207Pb/206Pb)c= 0.732 ± 0.0124
MSWD = 5.3, p(χ2) = 0
Age = 62.01 ± 0.45 / 2.1 Ma (n=14)
(207Pb/206Pb)c= 0.729 ± 0.0059
MSWD = 1.2, p(χ2) = 0.31
238U/206Pb

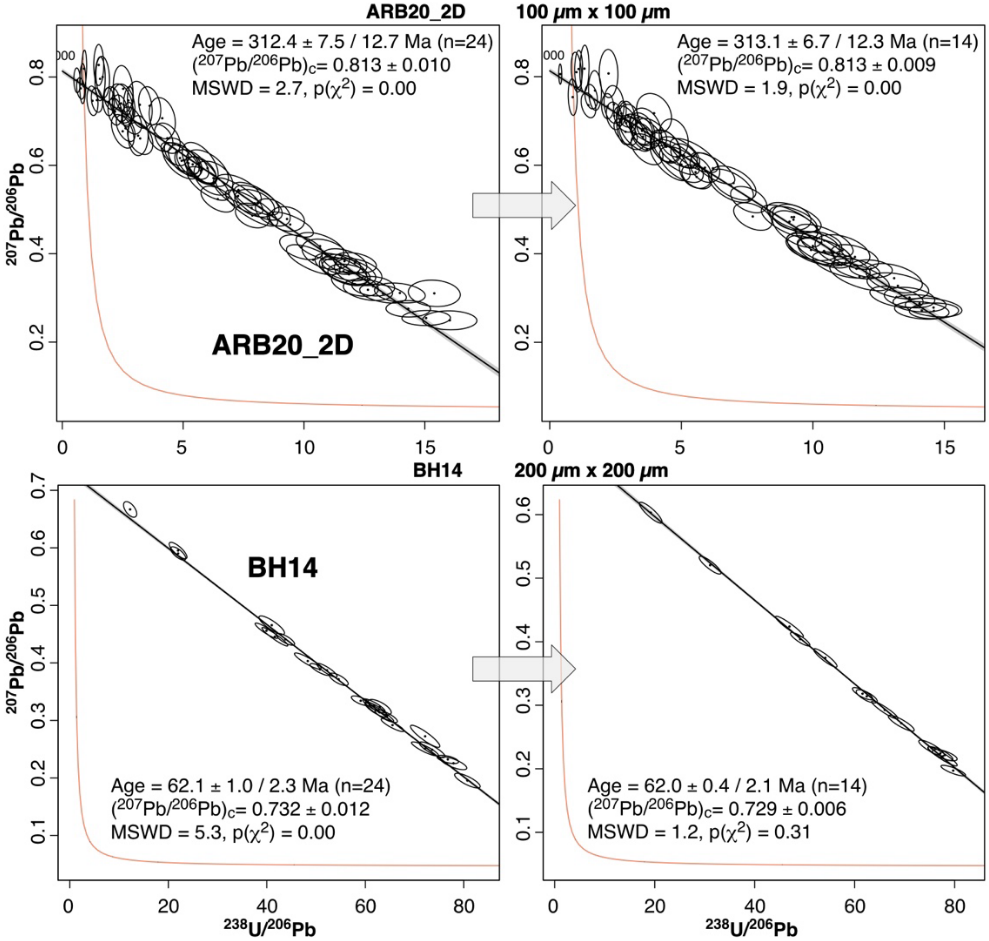

Figure 5~~4~~: Examples of ~~Tera-Wasserburg~~TW diagrams obtained for ARB20-2D and BH14 with the default grid position (left), and those corresponding to the best results in terms of precision and MSWD (right).

5.1.2 Case of low-U sample

In the case of samples with low U (and Pb) contents (C6-265-D5), the ages calculated from isotopic ~~image~~ maps are clearly biased. First, for 200 and 150 µm spots, the uncertainties on the ages obtained with the TW and ~~concordia~~ W regressions are high (higher than 15 Ma without propagation; Fig. 4, Table 3), and the ages vary widely (from 0 Ma to > 200 Ma). For ~~concordia~~ W regressions, they correspond to errorchrons in nearly all grid positions. For lower spot sizes, the ages obtained are not identical in the uncertainties (Fig. 3)~~,~~ and vary according to the spot size. They are much lower in the case of TW regressions than in that of ~~concordia~~ W ones (~~(~~Figs~~.~~ 3 and 6~~5~~A). The ages calculated by TW regression are centered around ~52-85 Ma (100 µm spots) and ~67-86 Ma (50 µm spots). ~~Concordia~~ W regression results in ages centered around ~93-155 Ma (100 µm spots) and ~93-119 Ma (50 µm spots) (Figs~~.~~ 3 and 6~~5~~C). These biased values are clearly related to the low number of counts in U and Pb, which induces a large dispersion of isotope ratios (Fig. S2). They mostly result in high MSWD values. These inconsistencies are resolved by averaging the number of mass sweeps on the time-resolved signal before data processing (equivalent to averaging the number of pixels along each linear scan), as done by Drost et al. (2018) and Hoareau et al. (2021) (Fig. 6~~5~~B). As shown in Fig. 6~~5~~C, the mean TW and ~~concordia~~ W ages evolve as a function of the number of averaged pixels, reaching identical values in their uncertainties from a value of 2, and a more restricted range from a value of 3. We note that the calculated average values vary slightly depending on the chosen spot size (~110-120 Ma for 100 µm and ~100-110 Ma for 50 µm). Despite their high uncertainties, these ages are consistent with the geological evidence of precipitation in the interval between ~112~~20~~ and ~101~~0~~ Ma (Pyrenean rifting; Motte et al., 2021). However, it is not possible to definitely ensure that the obtained ages truly reflect the precipitation age of the analysed dolomite. Therefore, it is necessary to test pixel averaging on samples that yield results similar to those of C6-265-D5 (i.e., differing ages depending on the concordia diagram used, due to low U and/or Pb concentrations), but for which the precipitation age is independently known from other methods.

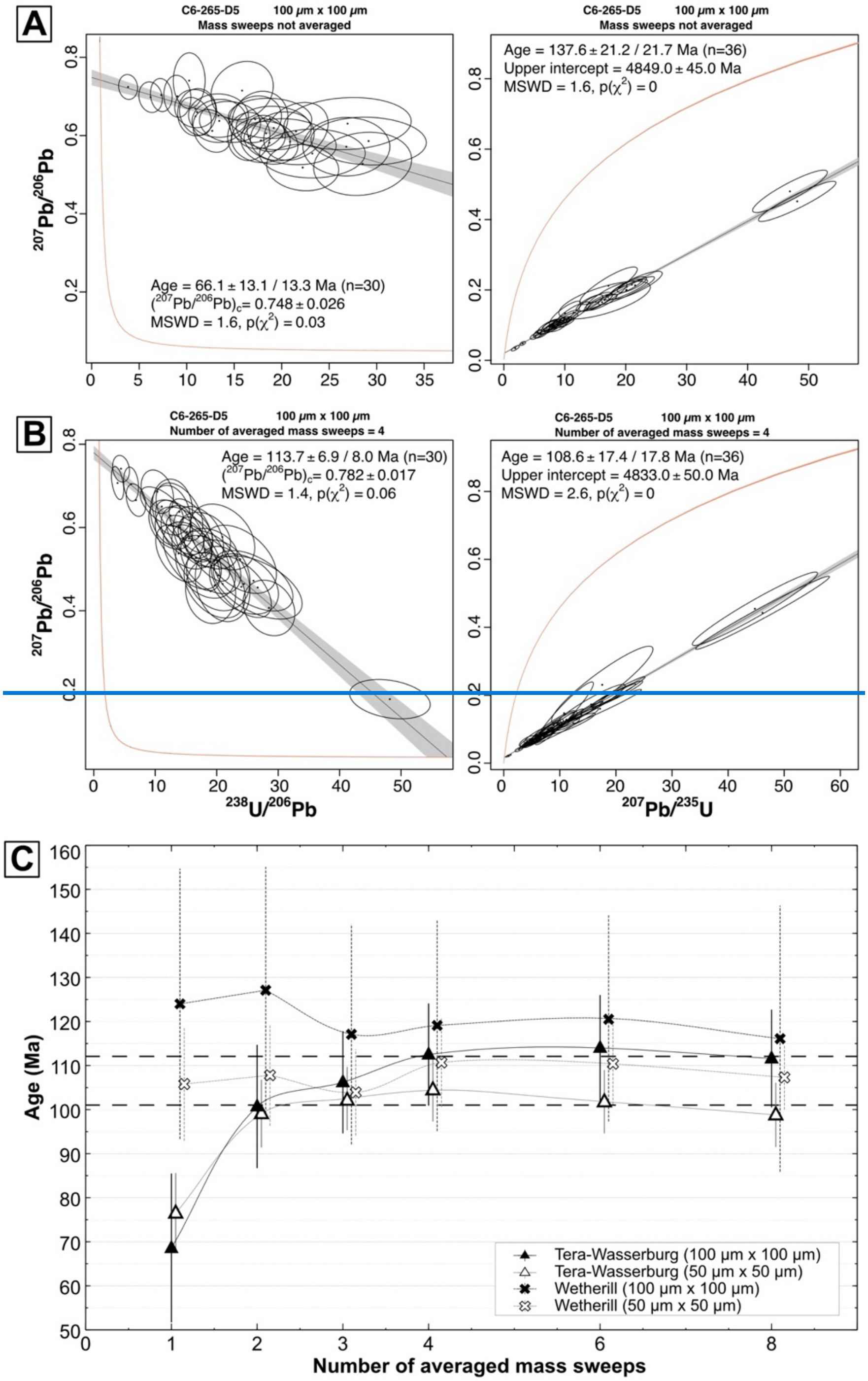
A
C6-265-D5 100 μm x 100 μm
Mass sweeps not averaged
Age = 66.1 ± 13.1 / 13.3 Ma (n=30)
(^{207}Pb/^{206}Pb)$_c$ = 0.748 ± 0.026
MSWD = 1.6, p(χ^2) = 0.03
Age = 137.6 ± 21.2 / 21.7 Ma (n=36)
Upper intercept = 4849.0 ± 45.0 Ma
MSWD = 1.6, p(χ^2) = 0
B
C6-265-D5 100 μm x 100 μm
Number of averaged mass sweeps = 4
Age = 113.7 ± 6.9 / 8.0 Ma (n=30)
(^{207}Pb/^{206}Pb)$_c$ = 0.782 ± 0.017
MSWD = 1.4, p(χ^2) = 0.06
Age = 108.6 ± 17.4 / 17.8 Ma (n=36)
Upper intercept = 4833.0 ± 50.0 Ma
MSWD = 2.6, p(χ^2) = 0
^{207}Pb/^{206}Pb
^{238}U/^{206}Pb
^{207}Pb/^{235}U
C
Age (Ma)
Number of averaged mass sweeps
Tera-Wasserburg (100 µm x 100 µm)
Tera-Wasserburg (50 µm x 50 µm)
Wetherill (100 µm x 100 µm)
Wetherill (50 µm x 50 µm)

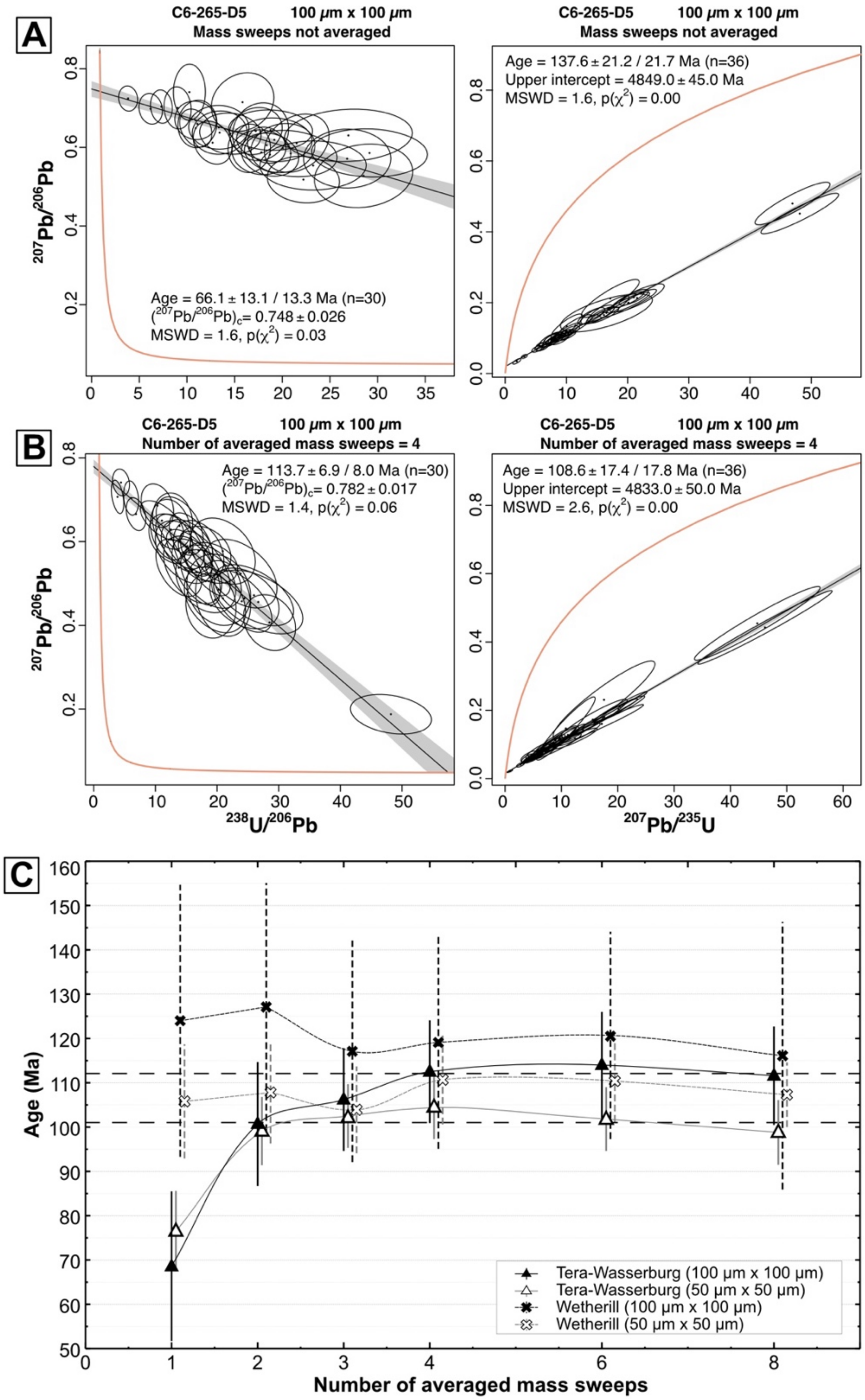

Figure 65: A. Best age results obtained for C6-265-D5 sample, with virtual spot sizes of 100 µm x 100 µm and no mass sweep averaging (left: TW diagram; right: Wetherill diagram). B. Same as A but with four averaged mass sweeps. C. Evolution of the weighted mean age calculated from several grid positions and for several virtual spot sizes (50 µm x 50 µm and 100 µm x 100 µm), as a function of the number of averaged mass sweeps, for sample C6-265-D5. The vertical bars correspond to 95% standard deviation. The expected age is between 1010 and 11220 Ma (dashed lines).

5.2 Ages calculated with the 'Rectis' method

Using the Rectis method as a complement to the 'mobile grid' method also yields very satisfactory results for high-U samples. In accordance with the theory for a sample of homogeneous age, the representation of all possible ellipses in a TW diagram defines a linear trend, with MSWD values close to or below 1 (Figs. 7~~6~~B and S5). The ages obtained by orthogonal regression through the set of virtual spots are identical to the expected ones. After selecting the maximum number of non-adjacent 100 µm or 50 µm spots on an ~~image~~ map (starting from the 50% spots closest to the regression line), expected ages are also obtained with IsoplotR. For several samples (ARB20-2D, BH14, DBT, Senz7), besides the low MSWD values, the age uncertainties are better than those obtained by the mobile grid method (Fig. 7~~6~~C; Table 4). For AUG_B6 and Cot02a samples, however, they are higher. In these cases, the virtual spots selected by Rectis may correspond to less spread ellipses in a TW diagram, and/or greater individual uncertainties. Regarding C6-265-D5, a similar behaviour to that observed with the grid method is obtained. The orthogonal regression gives an age of 72.6 Ma in the TW diagram, with a high MSWD (2.8) indicating the poor alignment of all ellipses (Fig. 7~~6~~C). The corresponding age after selecting the virtual spots is 68.6 ± 9.8 Ma. With a W~~etherill~~ diagram, the ages are much higher (126.9 Ma for orthogonal regression and 126.1 ± 17.1 Ma after selection). Averaging the number of mass sweeps by 4 results in final ages of 120.3 ± 14.3 Ma and 112.3 ± 14.3 Ma (TW and W~~etherill~~ diagrams, respectively), values that are in better accordance with the expected age, while being associated with lower MSWD values (Fig. 7~~6~~D). It should be noted that in this case the uncertainties are also lower than those obtained using the mobile grid method. Once again, the age obtained for C6-265-D5 is consistent with geological constraints (Motte et al., 2021), but it needs to be confirmed using other dating methods, such as isotope dilution.

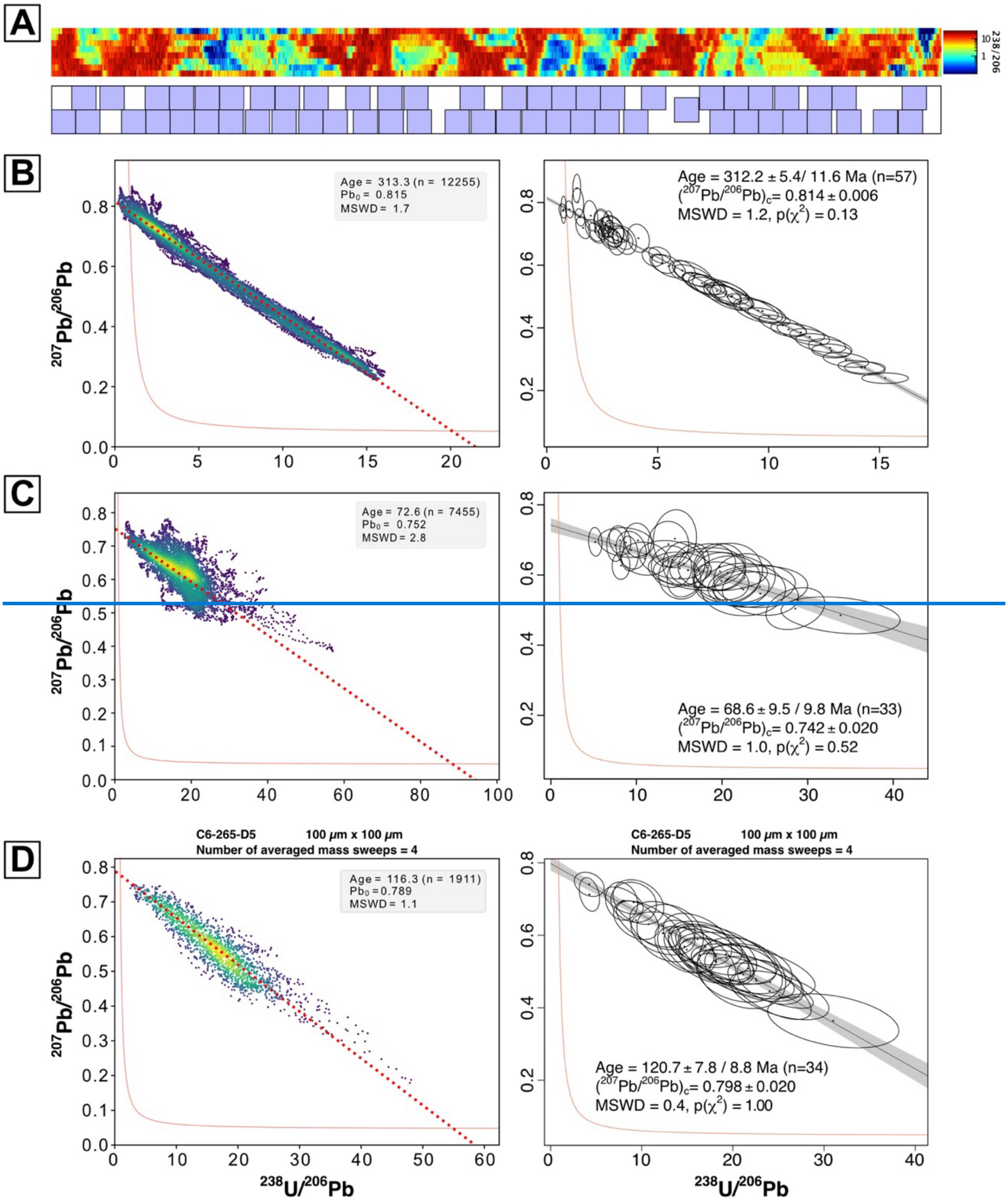
A
238/206
B
Age = 313.3 (n = 12255)
Pb0 = 0.815
MSWD = 1.7
207Pb/206Pb
Age = 312.2 ± 5.4/ 11.6 Ma (n=57)
(207Pb/206Pb)c = 0.814 ± 0.006
MSWD = 1.2, p(χ2) = 0.13
C
Age = 72.6 (n = 7455)
Pb0 = 0.752
MSWD = 2.8
Age = 68.6 ± 9.5 / 9.8 Ma (n=33)
(207Pb/206Pb)c = 0.742 ± 0.020
MSWD = 1.0, p(χ2) = 0.52
D
C6-265-D5 100 µm x 100 µm
Number of averaged mass sweeps = 4
Age = 116.3 (n = 1911)
Pb0 = 0.789
MSWD = 1.1
Age = 120.7 ± 7.8 / 8.8 Ma (n=34)
(207Pb/206Pb)c = 0.798 ± 0.020
MSWD = 0.4, p(χ2) = 1.00
238U/206Pb

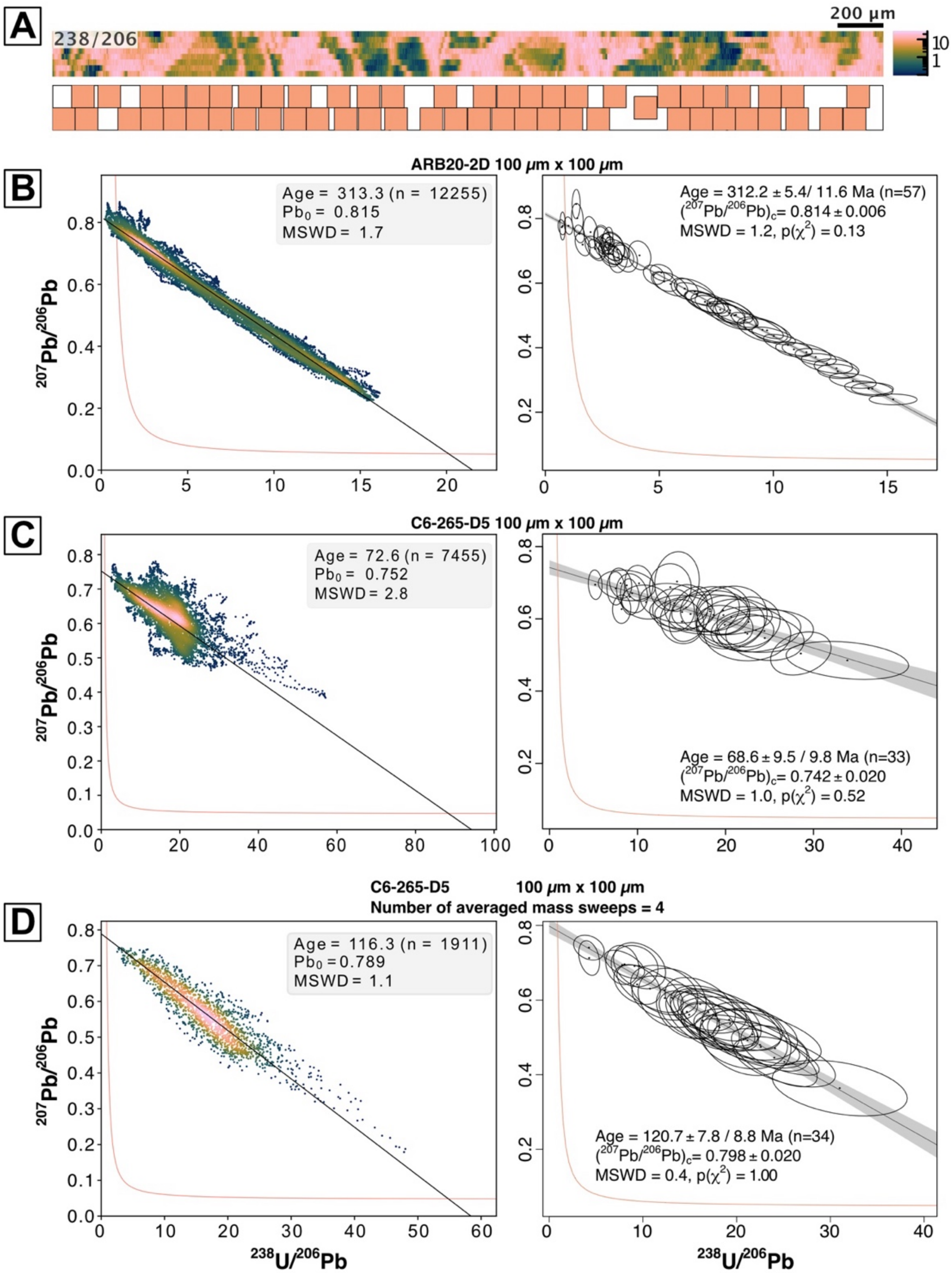

Figure 76: A. $^{238}U/^{206}Pb$ map of ARB20-2D, and location of the maximum number of non-adjacent 100 µm x 100 µm spots as calculated with the Rectis method. B. Results obtained for ARB20-2D sample. Left: TW diagram built from all possible 100 µm x 100 µm virtual spot positions on the ~~image~~map (uncertainties not represented). Age, common Pb and MSWD values are calculated from *Scipy* ODR regression. Right: Age result obtained from the maximum number of non-adjacent spots using the Rectis method, starting from the 50% spots closest to the ODR regression line. C. Same as B but for C6-265-D5 sample. D. Same as C but with four averaged mass sweeps. See text for details.

		Orthogonal regression (all possible virtual spots)				Results from best virtual spot location			
Sample name	Virtual spot size (µm)	Number of virtual spots	Age (Ma)	Pb0	MSWD	Number of virtual spots	Age (without/with systematic uncertainty) (Ma)	Pb0	MSWD
ARB20-2D	100 x 100	12255	313.3	0.815	1.7	57	312.2 ± 5.4 / 11.6	0.814 ± 0.006	1.2
AUG-B6	50 x 50	4417	43.5	0.853	1.4	61	44.1 ± 1.8 / 2.4	0.862 ± 0.016	0.7~~1~~
BH14	100 x 100	5627	62.2	0.730	0.8	47	62.2 ± 0.4 / 2.1	0.731 ± 0.004	0.84
C6-265-D5	100 x 100	7455	72.6	0.752	2.8	33	68.6 ± 9.5 / 9.8	0.742 ± 0.020	1.0
Cot2a (late fracture)[a]	25 x 25	1817	12.9	0.822	1.4	112	13.9 ± 3.2 / 3.2	0.825 ± 0.003	0.3~~28~~
DBT (anchored to 0.740)	100 x 100	2522	63.3	0.740	1.2	27	63.4 ± 0.8 / 2.3	0.74	0.3~~0~~
Senz7 (self corrected)[b]	50 x 50	5887	147.2	0.831	0.7	81	147.3 ± 2.3 / 5.4	0.830 ± 0.033	0.2~~2~~

Table 4: Age and common Pb values obtained with the Rectis method, using the TW regression. The results presented are those obtained by orthogonal regression (ODR) across all possible virtual spots, and after selecting the maximum number of non-adjacent spots on an ~~image~~ map. [a]Uncertainties greater than 20% filtered out; [b]based on 50 µm x 50 µm virtual spots.

5.3 Calculation of ages from very small areas

5.3.1 Manual selection of cement phases (Cot02a)

The isotopic ~~image~~ mapping obtained on sample Cot02a suggests the presence of several generations of calcite in addition to detrital quartz grains (Fig. 8A). In particular~~deed~~, U and Th concentration maps highlight 2 distinct calcite generations carrying the highest U/Pb ratios, which were manually selected using Iolite4 (Fig. 8~~7~~A). The first phase (Cal1) consists of 2 grains adjacent to quartz, covering a total area of approximately 0.064 mm^2 (equivalent to ~6 static spots of 100 µm in diameter), or ~2200 pixels. The average U content is 1.5 ± 0.03 ppm. The second cement phase (Cal2) fills a late fracture of about 50 µm wide, cutting across the previous phases as well as the quartz. The total selected area is approximately 0.092 mm^2 (i.e., ~9 static spots of 100 µm in diameter), or ~3800 pixels. U contents are high, with an average value of 6.9 ± 0.2 ppm.

For the first phase, the $^{238}U/^{206}Pb$ ratios are very low, resulting in very high uncertainties in the calculated TW ages (~25-40 Ma for ages centred around ~110-140 Ma, for virtual spots of 50 µm) (Fig. 8~~7~~B). As previously described for other samples, W ages are more scattered than TW ages, and also present higher individual uncertainties (Fig. 3). While most W ages are similar to TW ages when considering these uncertainties, the presence of errorchrons confirms that dating this generation remains a challenge. As before, reducing the size of the virtual spots and therefore increasing their number helps decrease the age uncertainty, which nevertheless remains above 15 Ma for 25 µm spots (TW diagrams). Since virtual spots may only partially overlap the selected areas, the number of spots may exceed what is expected based on the ratio between the selected cement surface area and the virtual spot area. Thus, it is possible to obtain up to 135 spots or 270 spots of 25 µm x 25 µm or 12.5 µm x 25 µm, respectively, on the selected surface, but with individual uncertainties in the $^{238}U/^{206}Pb$ and $^{207}Pb/^{206}Pb$ ratios that can sometimes exceed 50%. Filtering out uncertainties above 20% (as example) reduces the final number of spots but allows obtaining close age values regardless of the position of the virtual grid (~90-110 ± 20 Ma) (Fig. 8~~7~~B, 8~~7~~C). Additionally, filtering out spots containing too many pixels outside the selected zone (i.e., spots partially overflowing from this zone and thus with a high number of unused pixels) results in close results, but with MSWD values closer to unity (Fig. 8~~7~~C). Due to low $^{238}U/^{206}Pb$ values, such ages are roughly consistent with the stratigraphic age of the host carbonate (Coniacian-Santonian, i.e. 90-84 Ma). However, a more precise TW age of 83.0~~2~~ Ma ± 7.5~~6~~ Ma was obtained from similar grains from another ~~image~~map made on the same sample (~~not presented here~~Fig. S6), suggesting that in fact depositional carbonate or early calcite cement ~~was~~ may have been remobilized by the shear band formed during the Pyrenean orogeny.

For the second cement phase, a similar methodology yields much more recent TW ages (~12-14 Ma), in accordance with the petrographic evidence of late-stage fracturing (Fig. 8~~7~~D). Once again, W ages exhibit significantly greater dispersion and lower precision compared to TW ages, which are preferred (Fig. 3). It is interesting to note that for very small spot sizes (e.g., 12.5 µm x 25 µm), filtering out spots with uncertainties in the ratios above, for example, 10% logically reduces the number of spots significantly (from 436 to 32), but provides TW age uncertainties around 2 Ma, which are generally comparable to those obtained when all spots are retained (Fig. 7E). This allows testing various configurations (virtual spot sizes, filtering or not, grid migration) to find the parameters that yield the most reliable ages possible.

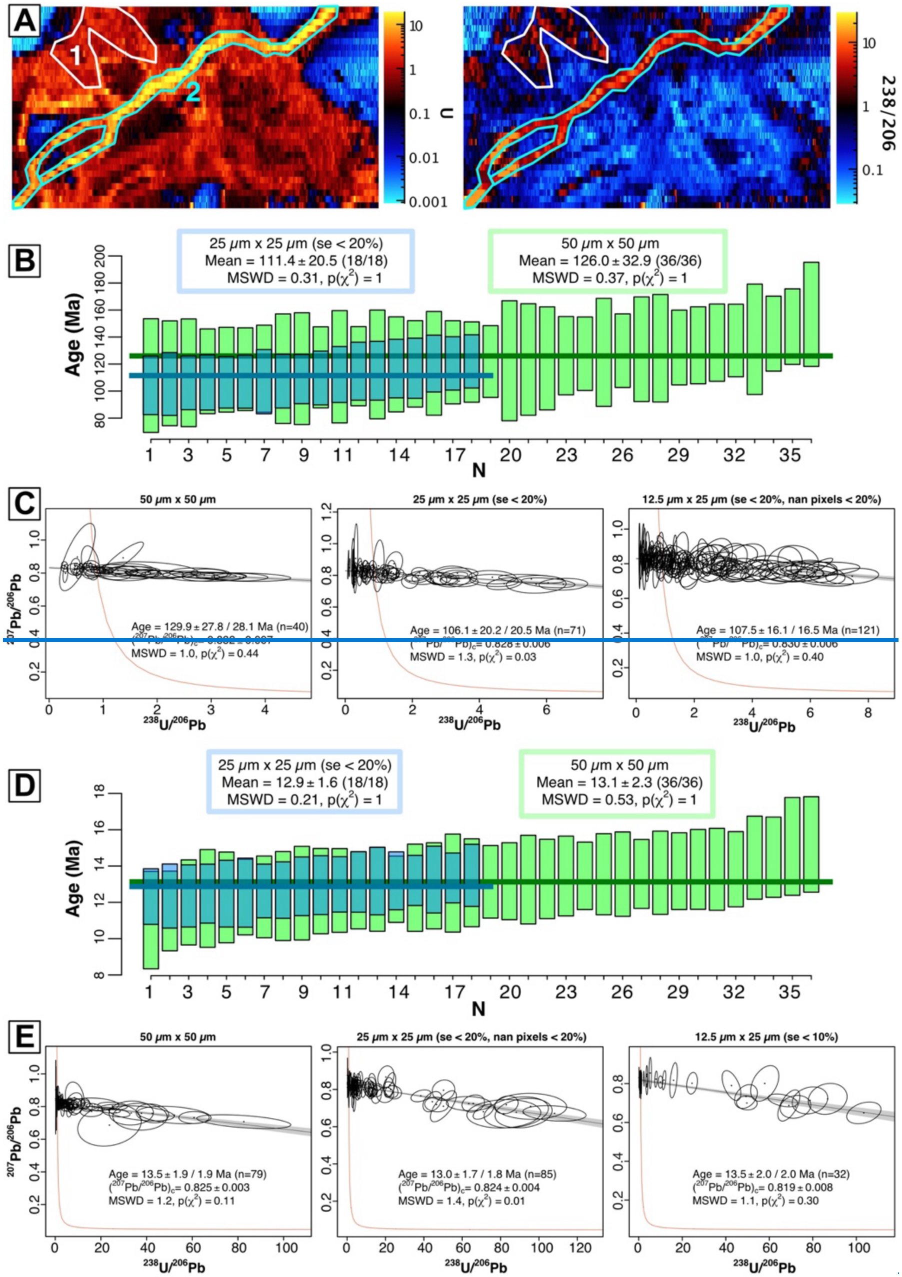
A
1
2
10
1
0.1
0.01
0.001
U
10
1
0.1
238/206
B
25 μm x 25 μm (se < 20%)
Mean = 111.4 ± 20.5 (18/18)
MSWD = 0.31, p(χ²) = 1
50 μm x 50 μm
Mean = 126.0 ± 32.9 (36/36)
MSWD = 0.37, p(χ²) = 1
Age (Ma)
N
C
50 μm x 50 μm
Age = 129.9 ± 27.8 / 28.1 Ma (n=40)
MSWD = 1.0, p(χ²) = 0.44
25 μm x 25 μm (se < 20%)
Age = 106.1 ± 20.2 / 20.5 Ma (n=71)
MSWD = 1.3, p(χ²) = 0.03
12.5 μm x 25 μm (se < 20%, nan pixels < 20%)
Age = 107.5 ± 16.1 / 16.5 Ma (n=121)
MSWD = 1.0, p(χ²) = 0.40
207Pb/206Pb
238U/206Pb
D
25 μm x 25 μm (se < 20%)
Mean = 12.9 ± 1.6 (18/18)
MSWD = 0.21, p(χ²) = 1
50 μm x 50 μm
Mean = 13.1 ± 2.3 (36/36)
MSWD = 0.53, p(χ²) = 1
Age (Ma)
N
E
50 μm x 50 μm
Age = 13.5 ± 1.9 / 1.9 Ma (n=79)
(207Pb/206Pb)c = 0.825 ± 0.003
MSWD = 1.2, p(χ²) = 0.11
25 μm x 25 μm (se < 20%, nan pixels < 20%)
Age = 13.0 ± 1.7 / 1.8 Ma (n=85)
(207Pb/206Pb)c = 0.824 ± 0.004
MSWD = 1.4, p(χ²) = 0.01
12.5 μm x 25 μm (se < 10%)
Age = 13.5 ± 2.0 / 2.0 Ma (n=32)
(207Pb/206Pb)c = 0.819 ± 0.008
MSWD = 1.1, p(χ²) = 0.30
207Pb/206Pb
238U/206Pb

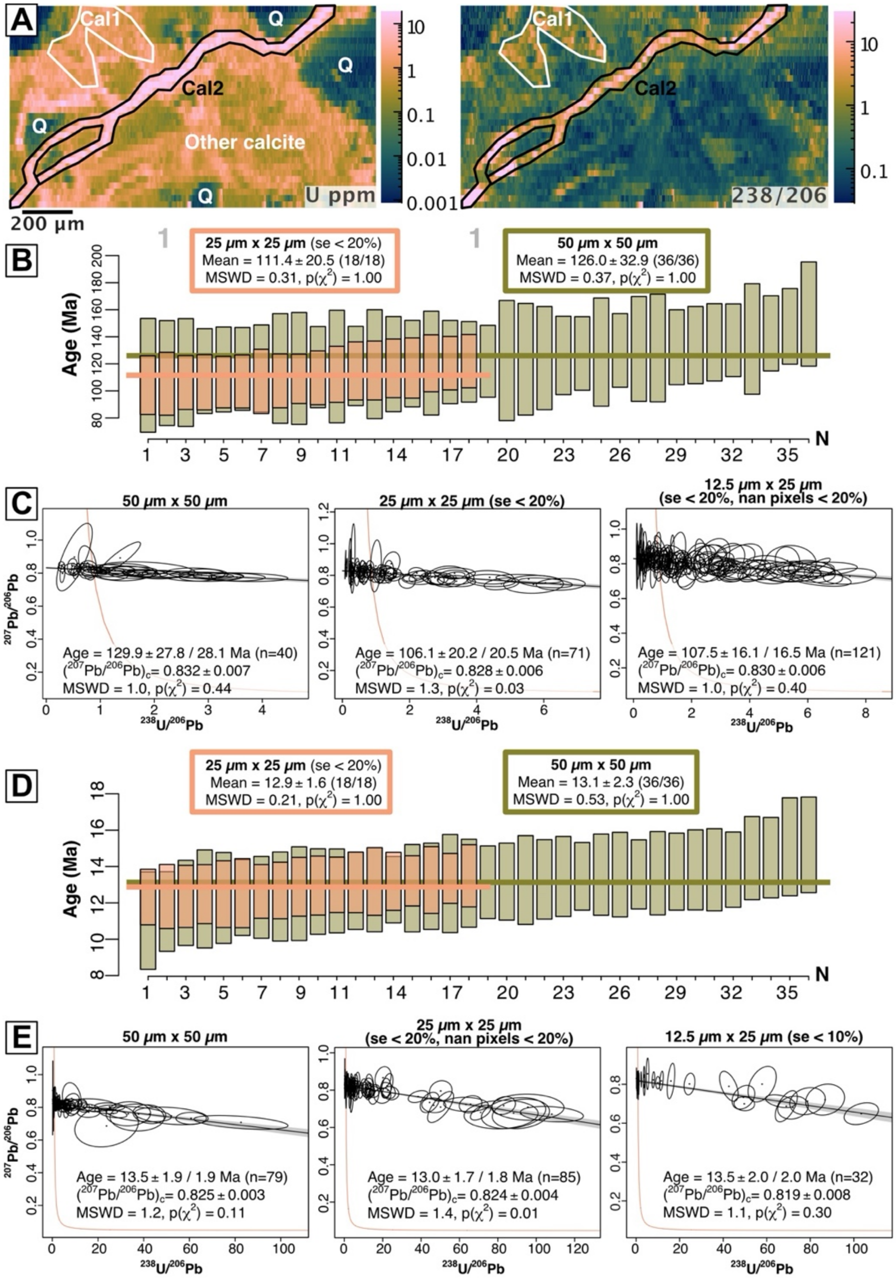

Figure 8~~7~~: A. LA-ICP-MS maps of U concentrations (in ppm), and $^{238}U/^{206}Pb$ ratios of sample Cot02a. The area highlighted in white ("Cal1") corresponds to the first generation of calcite, while the area highlighted in black~~lue~~ ("Cal2") corresponds to the second. Q: quartz; Other calcite: calcite with $^{238}U/^{206}Pb$ values too low to be datable. B. Weighted average of TW ages obtained for the first generation, for different grid positions and virtual spot sizes. In blue, spots with uncertainties greater than 20% have been filtered out. C. Best TW age results obtained for different virtual spot sizes, for the first generation. For 25 µm spots, spots with more than 20% of pixels outside the selected area (see fig. 8~~6~~A) are excluded, in addition to uncertainties greater than 20%. For 12.5 µm x 25 µm spots, the filtering is based on uncertainties greater than 10%. D. Same a B, but for the second generation. E. Same a C, but for the second generation. For 25 µm spots, spots with more than 20% of pixels outside the selected area and uncertainties greater than 20% are filtered out, while for 12.5 µm x 25 µm spots, spots with uncertainties greater than 10% are excluded.

5.3.2 Micro-~~image~~maps (‘sub-~~image~~map’ method) and weighted average of ages

Here we use the example of samples ARB20-2D and BH14, which are highly suitable for dating due to their high U content and good spread of ratio values, to demonstrate the possibility of obtaining ages from isotopic mapping of extremely small surfaces, comparable to that of a single spot in conventional LA-ICP-MS approach, and of calculating weighted mean ages for a larger ~~image~~map. The isotopic map obtained on ARB20-2D covers an area of ~0.72 mm^2 (20488 pixels), which corresponds to 18, 72, 290 and 1160 virtual spots of 200 µm, 100 µm, 50 µm and 25 µm on each side, respectively. By choosing a 25 µm grid, the map can then be divided, for example, into 18 sub-~~image~~maps of 200 µm x 200 µm, each containing 64 virtual spots of 25 µm x 25 µm, or into 72 sub-~~image~~maps of 100 µm x 100 µm, each containing 16 virtual spots (Fig. 9~~8~~A). In the case of 200 µm sub-~~image~~maps, the TW ages calculated for each sub-~~image~~map are mostly comparable to the age obtained from the entire ~~image~~map using 25 µm spots (~305.7 ± 3.3 / 8.7 Ma) within the limits of uncertainties, with uncertainties that can be below 10%. The weighted mean age (306.6 ± 3.1 Ma without propagated uncertainties) is also identical to the expected age (Fig. 9~~8~~B). The precision of the ages can be improved by choosing even smaller spot sizes (12.5 µm x 25 µm), corresponding to 128 virtual spots per 200 µm x 200 µm sub-~~image~~map (Fig. 9~~8~~C). In this case, 90% of the ages have uncertainties below 10%, with a comparable weighted mean (300.0 ± 3.1 Ma). Additionally, choosing 50 µm virtual spots provides greater accuracy in the calculated ages. In the case of 100 µm sub-~~image~~maps, the obtained TW ages have higher uncertainties, but the weighted mean is close (307.0 ± 3.4 Ma and 301.1 ± 3.2 Ma for 25 µm x 25 µm and 12.5 µm x 25 µm spots, respectively; Fig. 9~~8~~B). However, it should be noted that in all cases, several ages from the sub-~~image~~maps differ from the expected age within the limits of uncertainties. By following the same procedure for sample BH14, the obtained ages for most sub-~~image~~maps are mostly identical to the expected age, with uncertainties generally better than 10% (Fig. 10~~9~~). The weighted means are also perfectly comparable to the expected age. Again, choosing 50 µm spots in 200 µm sub-~~image~~maps yields the most reliable results (all ages are comparable to the expected age). In conclusion, these examples show that for favourable samples (U > 1 ppm, variable U/Pb), dating from 100 µm or 200 µm ~~image~~maps is possible, with slightly lower precision and, to a lesser extent, accuracy compared to more conventional approaches. The calculation of weighted mean ages also allows controlling the quality of the age obtained from the isotopic maps.

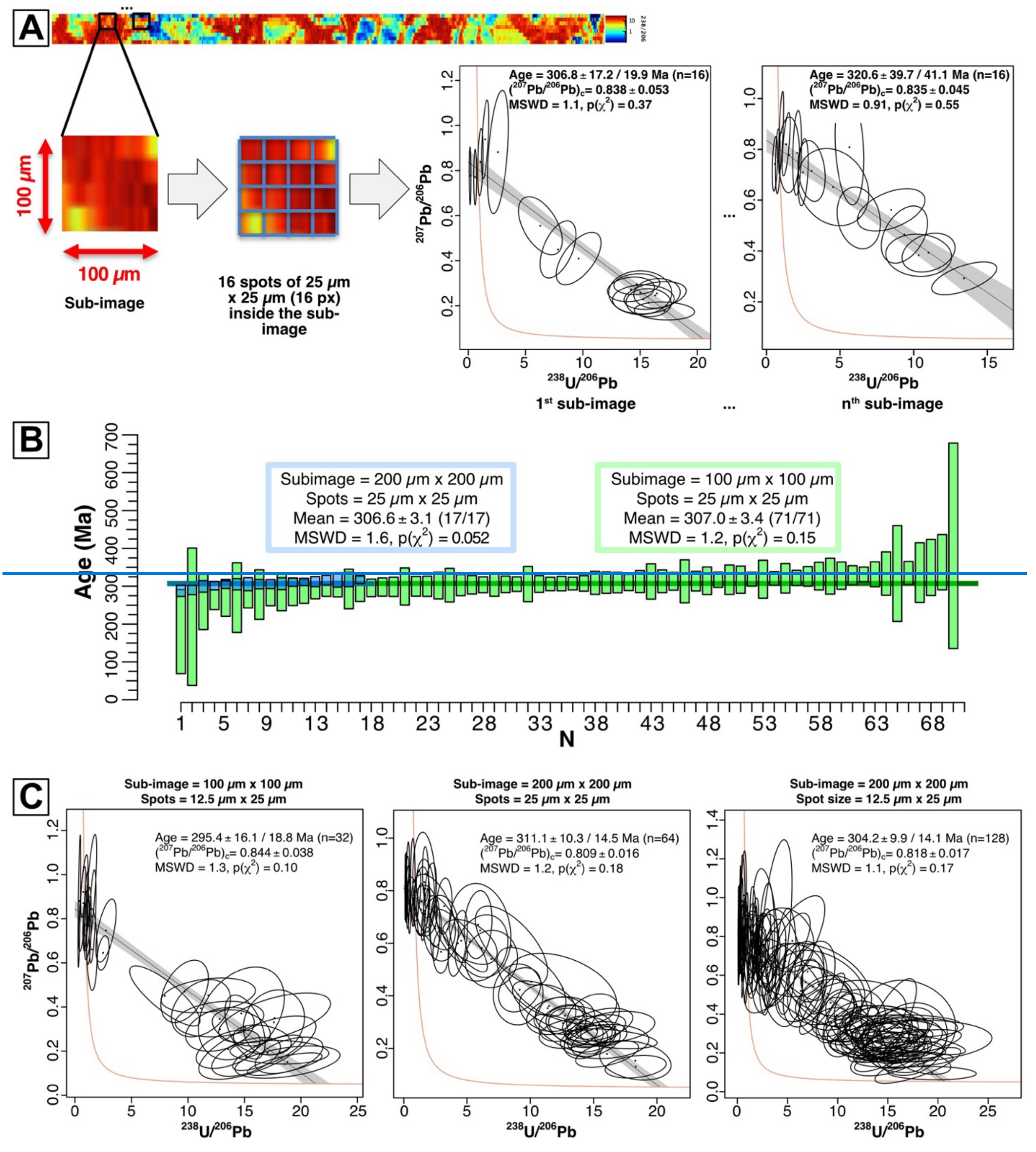
A
100 μm
100 μm
Sub-image
16 spots of 25 μm x 25 μm (16 px) inside the sub-image
Age = 306.8 ± 17.2 / 19.9 Ma (n=16)
(^{207}Pb/^{206}Pb)$_c$ = 0.838 ± 0.053
MSWD = 1.1, p(χ^2) = 0.37
Age = 320.6 ± 39.7 / 41.1 Ma (n=16)
(^{207}Pb/^{206}Pb)$_c$ = 0.835 ± 0.045
MSWD = 0.91, p(χ^2) = 0.55
^{207}Pb/^{206}Pb
^{238}U/^{206}Pb
1st sub-image
nth sub-image
B
Age (Ma)
Subimage = 200 μm x 200 μm
Spots = 25 μm x 25 μm
Mean = 306.6 ± 3.1 (17/17)
MSWD = 1.6, p(χ^2) = 0.052
Subimage = 100 μm x 100 μm
Spots = 25 μm x 25 μm
Mean = 307.0 ± 3.4 (71/71)
MSWD = 1.2, p(χ^2) = 0.15
N
C
Sub-image = 100 μm x 100 μm
Spots = 12.5 μm x 25 μm
Age = 295.4 ± 16.1 / 18.8 Ma (n=32)
(^{207}Pb/^{206}Pb)$_c$ = 0.844 ± 0.038
MSWD = 1.3, p(χ^2) = 0.10
Sub-image = 200 μm x 200 μm
Spots = 25 μm x 25 μm
Age = 311.1 ± 10.3 / 14.5 Ma (n=64)
(^{207}Pb/^{206}Pb)$_c$ = 0.809 ± 0.016
MSWD = 1.2, p(χ^2) = 0.18
Sub-image = 200 μm x 200 μm
Spot size = 12.5 μm x 25 μm
Age = 304.2 ± 9.9 / 14.1 Ma (n=128)
(^{207}Pb/^{206}Pb)$_c$ = 0.818 ± 0.017
MSWD = 1.1, p(χ^2) = 0.17

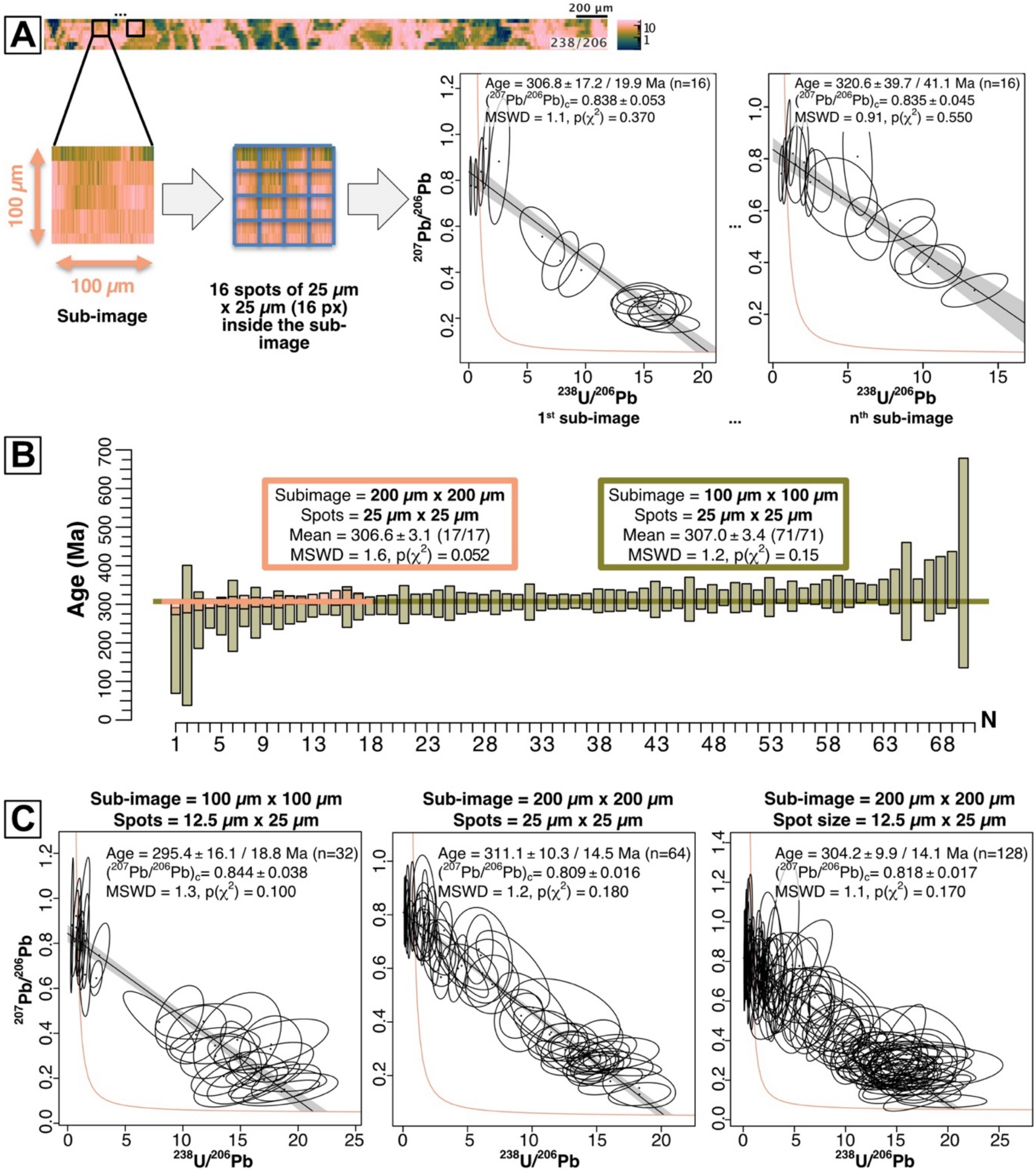

Figure 98: A. Scheme illustrating the procedure used to obtain ages from sub-~~image~~maps, based on ARB20-2D sample. A 100 µm x 100 µm (or 200 µm x 200 µm) ~~image~~map is extracted from the initial isotope map. It is itself discretised into small virtual spots (typically 25 µm x 25 µm). Two TW diagrams obtained from 2 different sub-~~image~~maps are shown as examples. B. Weighted averages of TW ages obtained from different sub-~~image~~maps for ARB20-2D, for 25 µm x 25 µm virtual spots. In blue, 200 µm sub-~~image~~maps and in green, 100 µm sub-~~image~~maps. Systematic uncertainties are not considered. C. TW diagrams of the best results obtained for different sub-~~image~~map and virtual spot sizes. Note the good distribution of ellipses despite the small size of the sub-~~image~~maps, and the similarity of the calculated ages.

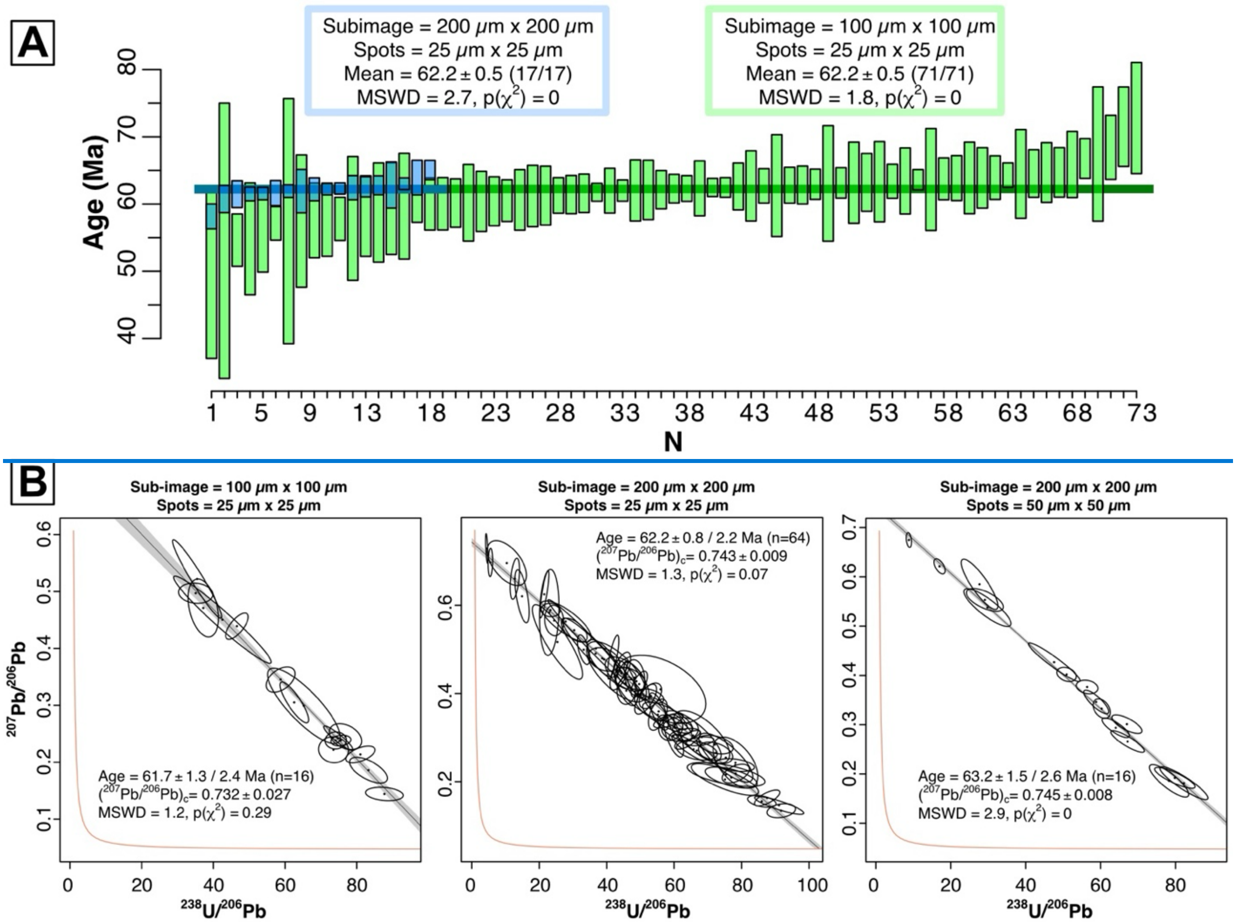
A
Subimage = 200 µm x 200 µm
Spots = 25 µm x 25 µm
Mean = 62.2 ± 0.5 (17/17)
MSWD = 2.7, p(χ2) = 0
Subimage = 100 µm x 100 µm
Spots = 25 µm x 25 µm
Mean = 62.2 ± 0.5 (71/71)
MSWD = 1.8, p(χ2) = 0
Age (Ma)
N
B
Sub-image = 100 µm x 100 µm
Spots = 25 µm x 25 µm
Age = 61.7 ± 1.3 / 2.4 Ma (n=16)
(207Pb/206Pb)c= 0.732 ± 0.027
MSWD = 1.2, p(χ2) = 0.29
Sub-image = 200 µm x 200 µm
Spots = 25 µm x 25 µm
Age = 62.2 ± 0.8 / 2.2 Ma (n=64)
(207Pb/206Pb)c= 0.743 ± 0.009
MSWD = 1.3, p(χ2) = 0.07
Sub-image = 200 µm x 200 µm
Spots = 50 µm x 50 µm
Age = 63.2 ± 1.5 / 2.6 Ma (n=16)
(207Pb/206Pb)c= 0.745 ± 0.008
MSWD = 2.9, p(χ2) = 0
207Pb/206Pb
238U/206Pb

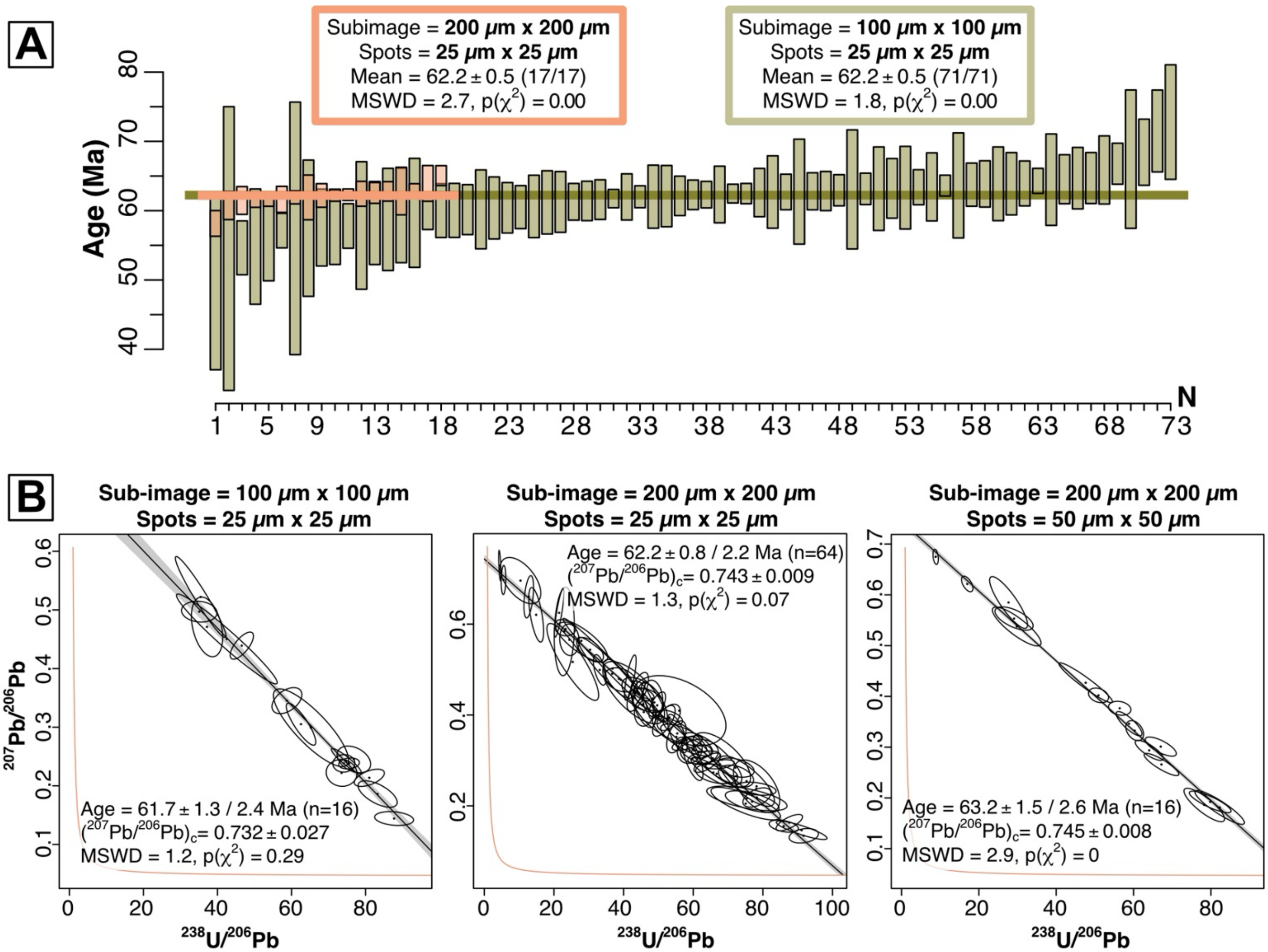

Figure 10~~9~~. A. Weighted averages of TW ages obtained from different sub-~~image~~maps for BH14, for 25 µm x 25 µm virtual spots. In blue, 200 µm sub-~~image~~maps and in green, 100 µm sub-~~image~~maps. Systematic uncertainties are not considered. B. TW diagrams of the best results obtained for different sub-~~image~~map and virtual spot sizes. Note the good distribution of ellipses despite the small size of the sub-~~image~~maps, and the similarity of the calculated ages.

6 Discussion

6.1 Interest and limitations of the ~~method~~virtual spot approach

The interest and inherent limitations of extracting ages from isotopic maps by LA-ICP-MS have already been addressed by several authors (Drost et al., 2018; Roberts et al., 2020; Hoareau et al., 2021; Davis and Rochín-Bañaga, 2021; Liu et al., 2023). One of the main advantages of isotopic maps, as detailed by Drost et al. (2018) and Roberts et al. (2020), is the ability to isolate pixels (either individually or as a range) based on their associated compositions or isotopic ratios, for example, to highlight multiple generations of cements or reject pixels with composition anomalies that may indicate detrital contamination before calculating one or more ages. Moreover, it is always possible to isolate ranges using co-localization approaches (Hoareau et al., 2021) or simply by manual selection in suitable software (here, Iolite4; see also Ansberque et al., 2020; Chew et al., 2021~~0~~). Various data processing methods for age calculations on carbonates have been proposed since the study by Drost et al. (2018). These include the pixel pooling method (Drost et al., 2018), robust regression on the values of the isotopic ratios of interest (Hoareau et al., 2021), as well as Bayesian regression (Davis and Rochín-Bañaga, 2021; Liu et al., 2023). As already discussed in the introduction, each approach has its advantages and disadvantages, and the present approach is no exception to this rule.

~~On the one hand, t~~The results presented here show that for samples traditionally favorable for U-Pb dating of carbonates by LA-ICP-MS (U > 100 ppb, good spread of U/Pb ratios of pixels), the virtual spot approach has several interesting advantages, especially when used on data obtained with a high repetition rate laser that allows high spatial resolutions (here, pixels of 25 µm x 1.3 µm), coupled with a high-sensitivity spectrometer (here, an SF-ICP-MS). In fact, it is possible, from isotopic maps typically obtained in less than 1 hour, to generate hundreds of virtual spots covering the selected carbonate phases with the 'mobile-grid' method. The ability to adjust the virtual spot size allows finding the most suitable combination in terms of statistics on the considered cement (low age uncertainty, MSWD close to 1), while avoiding possible accuracy biases through alternative approaches. The example of the Cot6a sample shows that robust ages are obtained on a mineralized fracture less than 50 µm thick, which would have been challenging to date with conventional static spot approaches. Here, the ability to generate more than 100 spots smaller than 50 µm is a notable advantage. Generally, spot sizes of 50 µm x 50 µm yield very satisfactory results. Another development presented here is the use of a mobile grid for virtual spots, which allows the user to calculate several tens of ages from the same ~~image~~map to evaluate their relevance, for example, through the visualization of their weighted means. In the case of reliable samples (i.e., with a homogeneous age and common Pb composition, sufficiently high U and Pb concentrations, and a wide enough range in isotopic ratios to allow for both accurate and precise U-Pb dating), it is expected that the position of the spots does not influence the calculated ages. It is then possible to choose the final age with the best statistical parameters. The Rectis method offers an alternative approach to age calculation that can results in even better statistical results. Finally, the approach can allow~~s~~ for age calculation from very small ~~image~~map dimensions (down to 100 µm x 100 µm) ('sub-map' method), although with the limitations presented with the examples of samples ARB20-2D and BH14. For larger ~~image~~maps, dividing them into sub-~~image~~maps allows the calculation of weighted mean ages, providing an additional way to evaluate the relevance of a cement age.

~~On the other hand~~However, the virtual spot approach is not flawless. First, the results obtained on sample C6-265-D5 show that a bias towards a too young age is possible when U and/or Pb concentrations are too low. It is then necessary to average the pixels (as done by Drost et al., 2018) and compare the ages obtained on TW and ~~concordia~~ W diagrams to obtain a satisfactory result, which can be laborious. Even with such pixel averaging, tests carried out on the ASH15 standard (Nuriel et al., 2021) failed to obtain a reliable age due to the very low Pb content of the sample (< 7 ppb), although this standard is used by several teams equipped with an identical mass spectrometer (e.g., Montano et al., 2021; Guillong et al., 2020). At the end of this study, it remains necessary to test additional samples with low U and Pb concentrations but independently known ages, in order to verify that pixel averaging yields accurate ages. T~~It therefore appears that t~~his problem of possible bias also requires further work on the conditions under which LA-ICP-MS ~~image~~maps are acquired, but~~.~~ our tests generally suggest that the comparison between TW and W results should be systematic, including in LA-ICP-MS U-Pb dating using static spots. Second, each virtual spot is obtained from adjacent pixels, rather than from the progressive ablation of the same surface as in the case of static spots. Given the variation of isotopic ratio values at the microscopic scale in carbonates, and despite signal mixing resulting from the washout time, it is expected that the uncertainty of the average obtained for each virtual spot will be larger. This limitation can be counterbalanced by using more virtual spots, as shown by the results obtained, for example, on samples BH14, DBT, AUG-B6, and ARB20-2D. Another counterintuitive effect of using virtual spots is the occurrence of high MSWD values for samples particularly favourable for dating, due to high error correlations. Sample BH14 is representative of this effect. For each virtual spot (100 µm x 100 µm), the variations in the $^{238}U/^{206}Pb$ and $^{207}Pb/^{206}Pb$ ratios are significant, resulting in high error correlations. This characteristic is likely to highlight minor heterogeneities in the sample. These indeed seem to exist in sample BH14 as shown by the MSWD value of 4.7 also obtained by Hoareau et al. (2021) with static spots of same size, higher than the value of 1.6 of Beaudoin et al. (2018). Note that this error correlation effect can also be considered as an additional means of better characterizing the sample in question, in favour of the approach presented here.

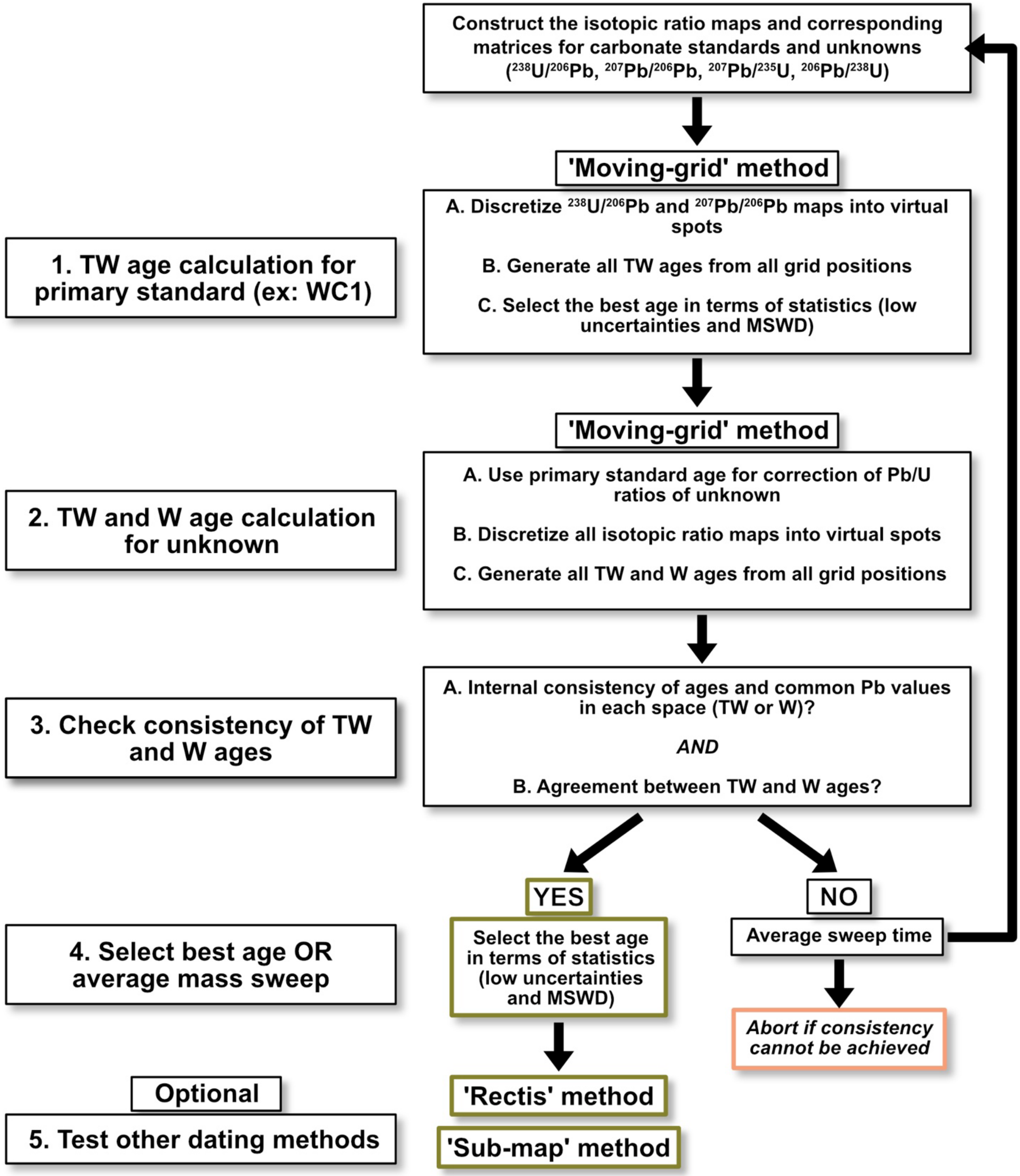

Figure 11. Guidelines for a proper use of the virtual spot approach.

6.2 Guidelines for a proper use of the approach

To use the virtual spot approach in the most effective and logical way—particularly considering the potential accuracy biases discussed earlier—we propose hereafter some guidelines, which are also summarized in Fig. 11. A detailed user guide is provided in the Zenodo repository. At this stage, we assume that the isotopic ratio maps and corresponding matrices of both standards and unknown-age samples have already been constructed using Iolite.

(1) Age calculation for primary standard ('moving-grid'). The first step is to calculate the uncorrected TW age of the primary standard (here, WC1). Under the analytical conditions of our study, a virtual spot size of 50 µm × 50 µm or 75 µm × 75 µm is appropriate. Thanks to the moving-grid approach, several dozen ages are generated, and the one with the best statistical parameters can be selected and used for the correction of unknown samples as well as secondary standards.

(2) Age calculation for the unknown sample ('moving-grid'). As with the primary standard, a series of ages is calculated for the unknown sample using the moving-grid method. By default, a virtual spot size of 100 µm × 100 µm is used, but other sizes may be chosen. At this stage, it is strongly recommended to perform age calculations in both TW and W concordia spaces.

(3) Check consistency ('moving-grid'): Assess (i) internal consistency of the age and common Pb values in each space (TW or W), and (ii) agreement between TW and W ages, within uncertainty limits. Both conditions must be satisfied. If not, one may investigate the potential causes (e.g., low U/Pb concentrations, insufficient isotopic ratio spread, multiple age populations).

(4) Selection of final age ('moving-grid') or mass sweep averaging:

(4a) If the ages are consistent, select the most statistically robust result (e.g., lowest MSWD, highest precision), potentially adjusting the virtual spot size to improve the results, and add external uncertainty onto the final age.

(4b) If the TW and W ages are inconsistent (as for C6-265-D5), recalculate the ages from the beginning after averaging the mass scans. If the TW and W results now converge, return to step 4a. If not, the sample is likely undatable.

(5) Optional steps (provided step 4 is successful):

(5a) Apply the 'Rectis' method to obtain a potentially more precise age or one with better statistical parameters;

(5b) Use the 'sub-map' method as an additional test. The weighted mean of the sub-map ages should ideally match the result obtained using the 'moving grid' method. Note that this method is expected to give satisfactory results only for appropriate samples (high U content and good spread of ratio values).

6.3~~2~~ Further developments

Further developments can be envisaged for the virtual spot method, to further enhance its appeal. A first major development will be to propose a routine that automatically selects virtual spots for maximum spread of isotope ratio values, for the number of virtual spots chosen by the user. This should lead to improved accuracy and precision of calculated ages. Other developments could include the automatic definition of virtual spots of variable size and shape, depending on the precision of the resulting isotope ratios, with a view to improving age calculations. Finally, in a more fundamental sense, the use of an average and its uncertainty implies that the distribution of pixel isotopic ratio values follows a normal distribution for each spot, which is probably valid only for the largest spots due to their higher number of pixels. The similarity and accuracy of the ages obtained here for different virtual spot sizes shows that skewed pixel values distribution does not introduce measurable bias into the results. However, additional tests must focus on using alternative statistics such as for example the median and its uncertainty.

7 Conclusion

The U-Pb carbonate dating approach from isotopic maps presented here takes benefit from the use of a high sensibility ICP-SF-MS coupled with a high-repetition-rate femtosecond ablation laser. The high ablation rate (> 100 Hz) enables the construction of ~~high spatial resolution~~ maps from lines of only 25 µm width. The maps ~~to be obtained, which~~ are then simply separated into a grid of virtual spots for the calculation of ages. Tests carried out on samples of known age show that the ages obtained correspond to reliable ages unbiased by the processing method. For samples with low U concentrations and noisy U/Pb and Pb/Pb ratios, comparison of the ages obtained from the TW and ~~concordia~~ W diagrams, together with smoothing of the number of pixels in the isotopic ~~image~~maps, seems to correct~~s~~ the bias towards ~~too young ages~~ inaccurate ages obtained from the unsmoothed maps. In addition to the advantages inherent to the use of isotopic maps described elsewhere (such as the possibility of filtering pixels or manually selecting regions of interest), the ability to move virtual spot grids implies that several ages can be obtained for the same study area, helping to assess their homogeneity. Finally, in the case of U-rich samples, we show that one can obtain reliable ages from very small ~~image~~maps (< 0.04 mm^2), paving the way for dating samples traditionally inaccessible to geochronology, such as micro-veins or micro-fossils. Although only tested on carbonates, there are no a priori limitations to the use of the virtual spot approach on other minerals traditionally used in U-Pb geochronology.

Appendix A

Table A1: Analytical conditions

Laboratory & Sample Preparation	
Laboratory name	Institut des sciences analytiques et de physico-chimie pour l'environnement et les matériaux (IPREM), UPPA, Pau (France)
Sample type/mineral	Calcite / dolomite
Sample preparation	In situ in polished blocks or thin sections (30 µm)
Imaging	Yes
Laser ablation system	

Make, Model & type	Lambda 3, Nexeya (France)
Ablation cell	Home-made (home-designed) two volumes ablation cell. The large cell has a rectangular shape and a volume of 11.25 cm^3 (75 x 25 x 6 mm size) while the small one, placed above the sample is of 10 mm diameter.
Laser wavelength (nm)	257 nm
Pulse duration (fs)	360 fs
Fluence ($J.cm^{-2}$)	5-8 $J.cm^{-2}$
Repetition rate (Hz)	100 or 500 Hz
Gas blank (s)	15 s per ~~image~~map (1 line)
Ablation duration (s)	38.3 to 145 s per line
Washout and/or travel time in between analyses (s)	Wash out time: ~1000 ms (Ar, October 2018) or ~500 ms (He, all other sessions). 15 vs or 25 s of break between lines to allow data processing.
Spot diameter (µm)	15 µm
Sampling mode / pattern	Ablation lines (25 µm-~~height~~width) made by combining laser beam movement across the surface (5 mm/s) and stage movement (25 µm/s). 25 µm between lines.
Cell Carrier gas (L/min)	He = 0.600 L/min
ICP-MS Instrument	
Make, Model & type	ICPMS Thermo Fisher ElementXR HR Jet Interface
RF power (W)	1000 - 1100W
Cooling gas flow rate	16 L min^{-1}
Auxiliary gas flow rate	1 L min^{-1}
Nebuliser gas flow rate	0.5 L min^{-1}
Masses measured	206, 207, 208, 232, 238
Samples per peak	30
Mass window	10 %
Sample time	3 ms

Settling time	1 ms
Mass sweep	57 ms (all masses, most samples) or 68 ms (all masses) or 134 ms (all masses)
Averaged mass sweep	No except C6-265-D5
Resolution	300
Sensitivity	Percentage of ions detected with regard to atoms ablated is ~0.04% for U, as calculated with NIST SRM 614
Data Processing	
Calibration strategy	Calibration by standard bracketing; NIST SRM 614 for Pb-Pb and WC-1 calcite for Pb-U
Reference Material info	Primary: NIST SRM 612 (before 2020) and NIST SRM 614 - Woodhead and Hergt (2001) WC-: 254.4 ± 6.4 Ma (2s) - Roberts et al., 2017 Secondary: Duff Brown 64.04 ± 0.67 Ma (2s) - Hill et al., 2016 AUG-B6 ~42.5 Ma – Pagel et al., 2018; Blaise et al., 2023
Data processing package used / Correction for LIEF	Element XR acquisition software, data processing with Iolite 4 and in-house Python/R code. Age determination through virtual spot discretization.
Common-Pb correction, composition and uncertainty	No common Pb correction. Ages in the figures are quoted at 95% absolute uncertainties and include systematic uncertainties (WC1 2.7%, decay constants 0.1%, long-term uncertainty 2%), propagation is by quadratic addition.
Quality control / Validation	3 analyses of Duff Brown (anchored to common Pb value of 0.74) gave ages of 62.6 ± 1.8 Ma, 60.7 ± 1.7 Ma, 65.9 ± 1.8 Ma. One analysis of AUG-B6 gave 42.2 ± 2.5 Ma.

Data availability.

The Supplementary material (methodology for LA-ICP-MS spot analyses, additional plots, pixel values of the isotopic ~~image~~maps and Python / R codes used for the data treatment) are publicly available in a Zenodo repository at https://doi.org/10.5281/zenodo.15582570~~10.5281/zenodo.12820356~~.

Supplement.

The supplement related to this article is available online at https://doi.org/10.5281/zenodo.1558257~~10.5281/zenodo.12820356~~.

Author contributions.

Guilhem Hoareau: Conceptualization, Data curation, Formal analysis, Investigation, Methodology, Project administration, Software, Supervision, Validation, Visualization, Writing - original draft, Writing - review & editing. **Fanny Claverie:** Investigation, Methodology, Resources, Project administration, Validation, Visualization, Writing - original draft, Writing - review & editing. **Christophe Pecheyran:** Conceptualization, Investigation, Methodology, Project administration, Supervision, Validation, Visualization, Writing - review & editing. **Gaëlle Barbotin:** Investigation, Methodology, Resources, Validation, Visualization. **Mickael Perk:** Data curation, Formal analysis, Methodology, Resources, Software, Writing - original draft, Writing - review & editing. **Nicolas E. Beaudoin:** Investigation, Resources, Validation, Visualization, Writing - original draft, Writing - review & editing. **Brice Lacroix**: Investigation, Resources, Validation, Writing - original draft, Writing - review & editing. **E. Troy Rasbury**: Formal analysis, Investigation, Resources, Validation, Visualization, Writing - original draft, Writing - review & editing

Competing interests.

The authors declare that they have no conflict of interest.

Review statement.

The authors would like to thank Don Davis, Barbara Kunz and Igor Figueiredo for their reviews that helped to greatly improve the manuscript. The Associate Editor Klaus Mezger is also warmly acknowledged.

Acknowledgements

The idea of a mobile grid came out after a discussion with Julien Mercadier (CNRS, Nancy) during the Spectratom 2022 congress in Pau. Pr. Joseph Mitchell (Stony Brooks University, New-York) is warmly thanked for fruitful discussion regarding the non-overlapping rectangle problem.

Financial support.

The samples were analyzed by LA-ICP-MS or ID-MS-ICP-MS as part of several projects not directly related to the present work, which was not supported by any funding.

References

Ansberque, C., Chew, D.M., and Drost, K.: Apatite fission-track dating by LA-Q-ICP-MS imaging. Chemical Geology, Volume 560, 119977, https://doi.org/10.1016/j.chemgeo.2020.119977, 2021.

Beaudoin, N., Lacombe, O., Roberts, N. M. W., and Koehn, D.: U-Pb dating of calcite veins reveals complex stress evolution and thrust sequence in the Bighorn Basin, Wyoming, USA, Geology, 46, 1015–1018, https://doi.org/10.1130/G45379.1, 2018.

Blaise, T., Augier, R., Bosch, D., Bruguier, O., Cogne, N., Deschamps, P., Guihou, A., Haurine, F., Hoareau, G., Nouet, J.: Characterisation and interlaboratory comparison of a new calcite reference material for U-Pb geochronology - The “AUG-B6” calcite-cemented hydraulic breccia. 2023 Goldschmidt Conference, 9-14 July, Lyon, France, 2023.

Brigaud, B., Bonifacie, M., Pagel, M., Blaise, T., Calmels, D., Haurine, F., and Landrein, P.: Past hot fluid flows in limestones detected by Δ47-(U-Pb) and not recorded by other geothermometers. Geology, 9(48), 851-856, https://doi.org/10.1130/g47358.1, 2020.

Chew, D., Drost, K., Marsh, J., and Petrus, J.: LA-ICP-MS imaging in the geosciences and its applications to geochronology. Chemical Geology, 559, 119917, https://doi.org/10.1016/j.chemgeo.2020.119917, 2021.

Chew, D., Petrus, J., and Kamber, B.: U–Pb LA–ICPMS dating using accessory mineral standards with variable common Pb. Chem. Geol., 363, 185-199, https://doi.org/10.1016/j.chemgeo.2013.11.006, 2014.

Chew, D.M., Petrus, J.A., Kenny, G.G., and McEvoy, N.: Rapid high-resolution U-Pb LA-Q-ICPMS age mapping of zircon. J. Anal. At. Spectrom. 32, 262–276, https://doi.org/ 10.1039/c6ja00404k, 2017.

CIAAW – IUPAC. http://www.ciaaw.org, accessed 24/05/2017

Cruset, D., Vergés, J., Rodrigues, N., Belenguer, J., Almar, Y., Pérez-Cáceres, I., and Messager, G.: U-Pb dating of carbonate veins constraining timing of beef growth and oil generation within Vaca Muerta Formation and compression history in the Neuquén Basin along the Andean fold and thrust belt. Mar. Petrol. Geol., 13, 105204, https://doi.org/10.1016/j.marpetgeo.2021.105204, 2021.

Davis, D., and Rochín-Bañaga, H.: A new bayesian approach toward improved regression of low-count U-Pb geochronology data generated by LA-ICPMS. Chemical Geology, (582), 120454. https://doi.org/10.1016/j.chemgeo.2021.120454, 2021.

Drost, K., Chew, D., Petrus, J., Scholze, F., Woodhead, J., Schneider, J., and Harper, D.: An image mapping approach to U-Pb LA-ICP-MS carbonate dating and applications to direct dating of carbonate sedimentation. Geochem. Geophys. Geosyst., 12(19), 4631-4648, https://doi.org/10.1029/2018gc007850, 2018.

Duffin, A., Hart, G., Hanlen, R., and Eiden, G.: Isotopic analysis of uranium in NIST SRM glass by femtosecond laser ablation MC-ICPMS. J. Radioanal. Nucl. Chem., 2(296), 1031-1036, https://doi.org/10.1007/s10967-012-2218-8, 2012.

Guillong, M., Wotzlaw, J.-F., Looser, N., and Laurent, O.: Evaluating the reliability of U–Pb laser ablation inductively coupled plasma mass spectrometry (LA-ICP-MS) carbonate geochronology: matrix issues and a potential calcite validation reference material, Geochronology, 2, 155–167, https://doi.org/10.5194/gchron-2-155-2020, 2020.

Ham, W.F.: Collings Ranch conglomerate, Late Pennsylvanian, in Arbuckle Mountains, Oklahoma, Amer. Assoc. Petrol. Geol. Bull., 38(9), 2035-2045, 1954.

Hill, C. A., Polyak, V. J., Asmerom, Y., and Provencio, P. P.: Constraints on a Late Cretaceous uplift, denudation, and incision of the Grand Canyon region, southwestern Colorado Plateau, USA, from U-Pb dating of lacustrine limestone, Tectonics, 35, 896-906, https://doi.org/10.1002/2016TC004166, 2016.

Hoareau, G., Claverie, F., Pecheyran, C., Paroissin, C., Grignard, P.-A., Motte, G., Chailan, O., and Girard, J.-P.: Direct U–Pb dating of carbonates from micron-scale femtosecond laser ablation inductively coupled plasma mass spectrometry images using robust regression, Geochronology, 3, 67–87, https://doi.org/10.5194/gchron-3-67-2021, 2021.

Hoareau, G., Claverie, F., pecheyran, C., Barbotin, G., Perk, M., Beaudoin, N., Lacroix, B., and Rasbury, T., Supplement to "The virtual spot approach: a simple method for image U-Pb carbonate geochronology by high-repetition rate LA-ICP-MS" by Hoareau et al (1.0.0) [Data set]. Zenodo. https://doi.org/10.5281/zenodo.15582570~~10.5281/zenodo.12820356~~, 2024.

Jochum, K.P., Weis, U., Stoll, B., Kuzmin, D., Yang, Q.C., Raczek, I., Jacob, D.E., Stracke, A., Birbaum, K., Frick, D.A., Gunther, D., and Enzweiler, J.: Determination of reference values for NIST SRM 610–617 glasses following ISO guidelines. Geostand. Geoanal. Res., 35(4), 397-429, doi:10.1111/j.1751908X.2011.00120.x, 2011.

Košler, J., 2008, Laser ablation sampling strategies for concentration and isotope ratio analyses by ICP-MS. In: Sylvester, P.J. (Ed.), Laser Ablation–ICP–MS in the Earth Sciences: Current Practices and Outstanding Issues. Mineralogical Association of Canada Short Course. 40. B.C., Vancouver, pp. 79–92.

Kylander-Clark, A. R. C.: Expanding the limits of laser-ablation U–Pb calcite geochronology, Geochronology, 2, 343–354, https://doi.org/10.5194/gchron-2-343-2020, 2020.

Liu, G., Ulrich, T., and Xia, F.: Brama: a new freeware python software for reduction and imaging of LA-ICP-MS data from U–Pb scans, J. Anal. At. Spectrom., 3(38), 578-586. https://doi.org/10.1039/d2ja00341d, 2023.

Ludwig, K. R.: User's manual for Isoplot version 3.75–4.15: a geochronological toolkit for Microsoft Excel, Berkeley Geochronological Center Special Publication, Berkeley, CA, USA, 2012.

Montano, D., Gasparrini, M., Rohais, S., Albert, R. K., and Gerdes, A.: Depositional age models in lacustrine systems from zircon and carbonate U-Pb geochronology, Sedimentology, 6(69), 2507-2534, https://doi.org/10.1111/sed.13000, 2021.

Motte, G., Hoareau, G., Callot, J., Révillon, S., Piccoli, F., Calassou, S., and Gaucher, E.: Rift and salt-related multi-phase dolomitization: example from the northwestern Pyrenees. Mar. Petrol. Geol., 126, 104932, https://doi.org/10.1016/j.marpetgeo.2021.104932, 2021.

Nuriel, P., Craddock, J., Kylander-Clark, A. R., Uysal, I. T., Karabacak, V., Dirik, R. K., Hacker, B. R., and Weinberger, R. J. G.: Reactivation history of the North Anatolian fault zone based on calcite age-strain analyses, Geology, 47, 465–469, 2019.

Nuriel, P., Wotzlaw, J.-F., Ovtcharova, M., Vaks, A., Stremtan, C., Šala, M., Roberts, N. M. W., and Kylander-Clark, A. R. C.: The use of ASH-15 flowstone as a matrix-matched reference material for laser-ablation U-Pb geochronology of calcite, Geochronology, 3, 35-47, https://doi.org/10.5194/gchron-3-35-2021, 2021.

Pagel, M., Bonifacie, M., Schneider, D., Gautheron, C., Brigaud, B., Calmels, D., and Chaduteau, C.: Improving paleohydrological and diagenetic reconstructions in calcite veins and breccia of a sedimentary basin by combining Δ47 temperature, δ^{18}Owater and U-Pb age, Chem. Geol., 481, 1-17. https://doi.org/10.1016/j.chemgeo.2017.12.026, 2018.

Paton, C., Woodhead, J. D., Hellstrom, J. C., Hergt, J. M., Greig, A., and Maas, R.: Improved laser ablation U-Pb zircon geochronology through robust downhole fractionation correction, Geochem., Geophy., Geosy., 11, Q0AA06, https://doi.org/10.1029/2009GC002618, 2010.

Paton, C., Hellstrom, J., Paul, B., Woodhead, J., and Hergt, J.: Iolite: Freeware for the visualisation and processing of mass spectrometric data. J. Anal. At. Spectrom., 26, 2508, doi:10.1039/c1ja10172b, 2011.

Roberts, N. M. W., Drost, K., Horstwood, M. S. A., Condon, D. J., Chew, D., Drake, H., Milodowski, A. E., McLean, N. M., Smye, A. J., Walker, R. J., Haslam, R., Hodson, K., Imber, J., Beaudoin, N., and Lee, J. K.: Laser ablation inductively coupled plasma mass spectrometry (LA-ICP-MS) U–Pb carbonate geochronology: strategies, progress, and limitations, Geochronology, 2, 33– 61, https://doi.org/10.5194/gchron-2-33-2020, 2020.

Subarkah, D., Nixon, A. L., Gilbert, S. E., Collins, A. S., Blades, M. L., Simpson, A., Lloyd, J. C., Virgo, G. M., and Farkaš, J.: Double dating sedimentary sequences using new applications of in-situ laser ablation analysis, Lithos, 480–481, 107649, https://doi.org/10.1016/j.lithos.2024.107649, 2024.

Roberts, N. M. W., Rasbury, E. T., Parrish, R. R., Smith, C. J., Horstwood, M. S. A., and Condon, D. J.: A calcite reference material for LA-ICP-MS U-Pb geochronology, Geochem., Geophy., Geosy., 18, 2807–2814, https://doi.org/10.1002/2016GC006784, 2017.

Roberts, N., and Holdsworth, R.: Timescales of faulting through calcite geochronology: a review, J. Struct. Geol., 158, 104578, https://doi.org/10.1016/j.jsg.2022.104578, 2022.

Rochín-Bañaga, H., Davis, D., and Schwennicke, T.: First U-Pb dating of fossilized soft tissue using a new approach to paleontological chronometry, Geology, 9(49), 1027-1031, https://doi.org/10.1130/g48386.1, 2021.

Taxopoulou, M. E., Beaudoin, N. E., Aubourg, C., Charalampidou, E. M., Centrella, S., & Saur, H.: How pressure-solution enables the development of deformation bands in low-porosity rocks, Journal of Structural Geology, 166, 104771, 2023.

Vermeesch, P., 2018, IsoplotR: a free and open toolbox for geochronology, Geosc. Frontiers, 9, 1479-1493, https://doi.org/10.1016/j.gsf.2018.04.001.

Woodhead, J. D. and Hergt, J. M.: Strontium, neodymium and lead isotope analyses of NIST glass certified reference materials: SRM 610, 612, 614, Geostandard. Newslett., 25, 261–266, https://doi.org/10.1111/j.1751-908X.2001.tb00601.x, 2001.

Woodhead, J., and Petrus, J.: Exploring the advantages and limitations of in situ U–Pb carbonate geochronology using speleothems, Geochronology, 1(1), 69-84, https://doi.org/10.5194/gchron-1-69-2019, 2019.